# Conformational Characterization and Controlled Processing of *Samia cynthia ricini* Silk Fibroin

**Doctoral dissertation**

Doctor of Engineering

Presented by

**Kelvin Moseti Okong'o**

Submitted to the
Tokyo University of Agriculture and Technology
2020

## Table of Contents

## Abbreviations and Acronyms

| | |
|---|---|
| AFM | Atomic force microscopy |
| CP/MAS | Cross-polarization magic angle spinning |
| DSC | Differential scanning calorimetry |
| fhc | fibroin heavy chain |
| flc | fibroin light chain |
| FTIR | Fourier transform infra-red spectroscopy |
| GPC | Gel permeation chromatography |
| HFA | hexafluoroacetone |
| HFIP | 1,1,1,3,3,3-hexafluoro-2-propanol |
| HPLC | High-performance liquid chromatography |
| JICA | Japan International Cooperation Agency |
| JST | Japan Science and Technology Agency |
| KALRO | Kenya Agricultural and Livestock Research Organization |
| kDa | kilodaltons |
| Mw | Molecular weight |
| NARO | National Agriculture and Food Research Organization |
| NMR | Nuclear magnetic resonance |
| NPAB | non-poly-L-alanine |
| OPA | *o*-phthalaldehyde |
| PAB | poly-L-alanine block |
| PMMA | polymethyl methacrylate |
| ppm | Parts per million |
| PTFE | polytetrafluoroethylene |
| RI | Refractive index |

| | |
|---|---|
| SATREPS | Science and Technology Research Partnership for Sustainable Development |
| SGF | Silk gland fibroin |
| TFA | trifluoroacetic acid |
| TG | Thermal gravimetry |
| TMS | tetramethyl silane |
| WAXD | Wide-angle X-ray diffraction |
| $\varepsilon$ | Strain |

# Chapter I

# Introduction

## 1.1. Silks

Silks are proteinaceous fibrous biopolymers secreted by various invertebrates, notably spiders and insects [1,2]. They exhibit unique properties, often presumed to be dictated by their function; these include predation (spider webs), housing (honeybees and wasps) and protection (silkworm cocoons) [1-4], among others. *Bombyx mori* (*B. mori*) and several wild silkworm species from the Saturniidae family, are major silk producers that have been explored for exploitation primarily as source of textiles. The domesticated *B. mori* silk is often referred to as mulberry silk [5], whereas the rest are referred to as non-mulberry or wild silks. Saturniidae wild silkworms include; *Samia cythia ricini* (*S. c. ricini*) [6], *Antheraea pernyi* (*A. pernyi*) [7,8], *Antheraea yamamai* (*A. yamamai*) [9], *Antheraea assama* (*A. assama*) [10], and *Antheraea mylitta* (*A. mylitta*) [11].

Silkworm silks consist of two main components; the hydrophobic fibroin core and hydrophilic sericin layer that glues a pair of fibroin filaments which constitute the major component of silk fibre [2,4]. *B. mori* silk fibroin consist of three components: fibroin heavy chain (fhc ~350 kDa), fibroin light chain (flc ~26 kDa) and P25 (~ 30 kDa), whereas saturnidae silk fibroins consist of one component, fibroin, that forms homodimers linked with a disulfide bond [2,4]. The primary structure of *B. mori* fhc [12] has been shown to mainly consist of a $(GAGAGS)_n$ repeat sequence, whereas the Saturniid's silk fibroins have been clarified to typically comprise of 93 alternating repeating motifs of the poly-L-alanine block (PAB), $Ala_{(12-13)}$, and Gly-rich, non-poly-L-alanine (NPAB) sequence regions [6-11].

Saturniid wild silks exhibit unique properties, even among species. This has been hypothesized to result from the high variability of the NPAB sequences among the silkworm species relative to the non-repetitive region of the fibroin sequences [8,13]. Such variability is anticipated to offer a potential source of a wide array of valuable biomaterials with promising applications. However, the determinants of these differences are not clear, and understanding their origin is highly desirable.

### 1.2. The biomedical use of silk

Biomaterials play a crucial role in regenerative medicine as scaffolds for cell proliferation and differentiation in order to promote healing of tissue lesion. Depending on the target tissue, scaffolds are often required to meet certain physical and biological properties. For example, bone and dental, corneal, and skin materials, will require scaffolds with high tensile strength, high transparency, and elasticity, respectively.

Currently, silks are widely regarded as model systems for high-performance polymeric materials owing to their exquisite balance of modulus, strength, extensibility, as well as biocompatibility, biodegradability and workability, properties that front them as potential sustainable sources of ecologically benign commercial polymers [4,5,16,17]. *B. mori* silkworm species is well known; It has been domesticated by man for centuries, during which its silk was primarily utilized for textile applications [4,5]. However, in the recent past, its utilization for non-textile applications, notably as a source of biomaterials, has substantially increased. Such applications include tissue engineering where it is used in different formats as a biomaterial that can potentially restore, maintain or improve tissue functions lost due to age, disease, damage or congenital defects [18]. Substantial advancements have been made as detailed in a recent review by Holland et al., [16]. These include clinical uses of *B. mori* silk as sutures, surgical meshes, and fabrics, as well as clinical trials in wound healing in various formats, such as silk solution, films, scaffolds, electrospun materials, hydrogels, and particles.

### 1.3. Use of wild silk in the development of biomaterials

Non-mulberry sericulture is a crucial undertaking world over, since besides the economic gains, it stands to enhance conservation of indigenous flora and fauna as well as serving as a positive multiplier effect on other ecological benefits such as: Control of deforestation and reforestation. The indigenous forests created could contribute to increased forest cover, enhanced production of environmental goods and services such as clean air, water and wind breaks, sources for ethnobotany materials, climate change management, bio-prospecting and other non-destructive uses such as bee keeping, tourism, photography, nature trails, and aesthetics, and can be used be used for carbon credit compensation [14,15].

Moreover, wild silks are also receiving increasing attention, especially in the biomedical field, owing to their impressive material properties, promising applications and abundance in nature [14,15,20-24]. For instance, the primary structures of some wild silk fibroins are known to contain functional sequences. This includes *A. pernyi* whose silk fibroin is known to contain the tripeptide sequence, Arg-Gly-Asp, believed to be a specific interaction site for cell attachment [21,22,23]. Due to these, attempts to regenerate wild silk fibroin proteins [20], blend them with *B. mori* silk fibroin to enhance cell attachment [23], as well as design of silk-like recombinant proteins incorporating the functional sequences [24] have been explored.

Despite the incredible advancements in the use of *B. mori* silk in the development of biomaterials, utilization of wild silk fibroin as remains scarce. This is primarily due to lack of appropriate processing technologies for wild silk fibroin, that is, the conventional processing strategies used in the processing of *B. mori* silk are not applicable in the processing of wild silks like *S. c. ricini*. In this study, fibroin from *S. c. ricini* silkworm silk, whose production is now domesticated and practiced in various countries world-over including Kenya [25], was

studied as a candidate fibroin for the development of a biomaterial with suitable properties for potential use in tissue engineering.

To utilize silk fibroin in the fabrication of biomaterials, it is necessary to convert them into adoptable morphologies or formats; some of which have been mentioned in the preceding sub-section. This often requires regeneration or reconstitution, which entails purification and dissolution of the silk proteins in appropriate solvents or co-solvents to obtain solutions from which the desired formats, dictated by the target applications, can be fabricated.

As already mentioned, the primary structure of *S. c. ricini* silk fibroin [6] is different and attempts to use the conventional solvents or solvent systems and strategies utilized in processing of *B. mori* silk fibroin have been largely unsuccessful [20]. Alternative approaches, including the use of aqueous solutions of liquid fibroin prepared from silk dope obtained directly from the lumen of posterior silk glands of mature larvae have been explored [26]. However, biomaterials fabricated from such solutions are water-soluble and often require post-treatment to render them water-stable for use in wet-state applications [27].

To efficiently utilize this promising bio-resource, detailed understanding its composition, structure, and properties is imperative. This understanding is anticipated to form the basis of the design and development of appropriate formats of *S. c. ricini* silk fibroin -based, and even silk-like (silk-inspired) biomaterials. Yoshioka et al recently devised a novel scheme of obtaining water insoluble $\alpha$-helix-rich films from *B. mori* silk fibroin which exhibited a good balance of mechanical properties [28]. Given that *S. c. ricini* silk fibroin is poly-L-alanine rich [6], an intrinsically $\alpha$-helix-stabilizing amino acid [29], then it is anticipated that it may be possible to fabricate a cast film that is $\alpha$-helix-rich and water-stable.. For this to be successful, understanding the structure and properties of *S. c. ricini* the silk is imperative.

*S. c. ricini* native fibre and silk fibroin, often as cast films, have been extensively characterised using various analytical tools including X-ray diffraction, infra-red, Raman and

high-resolution solid-state NMR spectroscopy [30-37]. Silk fibroin cast films are relatively a relatively simple format that can conveniently be generated from different solvents such as aqueous buffers, organic or ionic liquids through simple solvent evaporation [16,17,27,28,38,39] as well as printing [40]. They are particularly an interesting configuration and have attracted considerable attention since their inherent practical advantages are potentially adoptable for use in *in vitro* and *in vivo* degradation and drug release studies, wound dressing and optical applications such as contact lenses, among others [16,17]. However, most conventional cast films are $\beta$-sheet-rich, often induced by post-treatments to render them stable, which in turn diminishes their desirable inherent properties such as flexibility [20,27,38].

### 1.4. Purpose of this study

In view of the highlighted challenge, the purpose of this research was to prepare a $\alpha$-helix-rich and water-insoluble film from *S. c. ricini* silk fibroin. To attain these, first it was necessary to understand some aspects of *S. c. ricini* silks that are yet to be clarified and considered useful regarding the mechanical properties of the desired film. This include the aggregation state of residual $\alpha$-helix domains and their influence on the physical properties of *S. c. ricini* native fiber. Moreover, the secondary structure of the silk proteins is dependent on the initial solvent and therefore controllable. For instance, fluorinated solvents such as 1,1,1,3,3,3-hexafluoro-2-propanol (HFIP) and hexafluoroacetone (HFA) induce $\alpha$-helical structure in silk proteins [41,42].

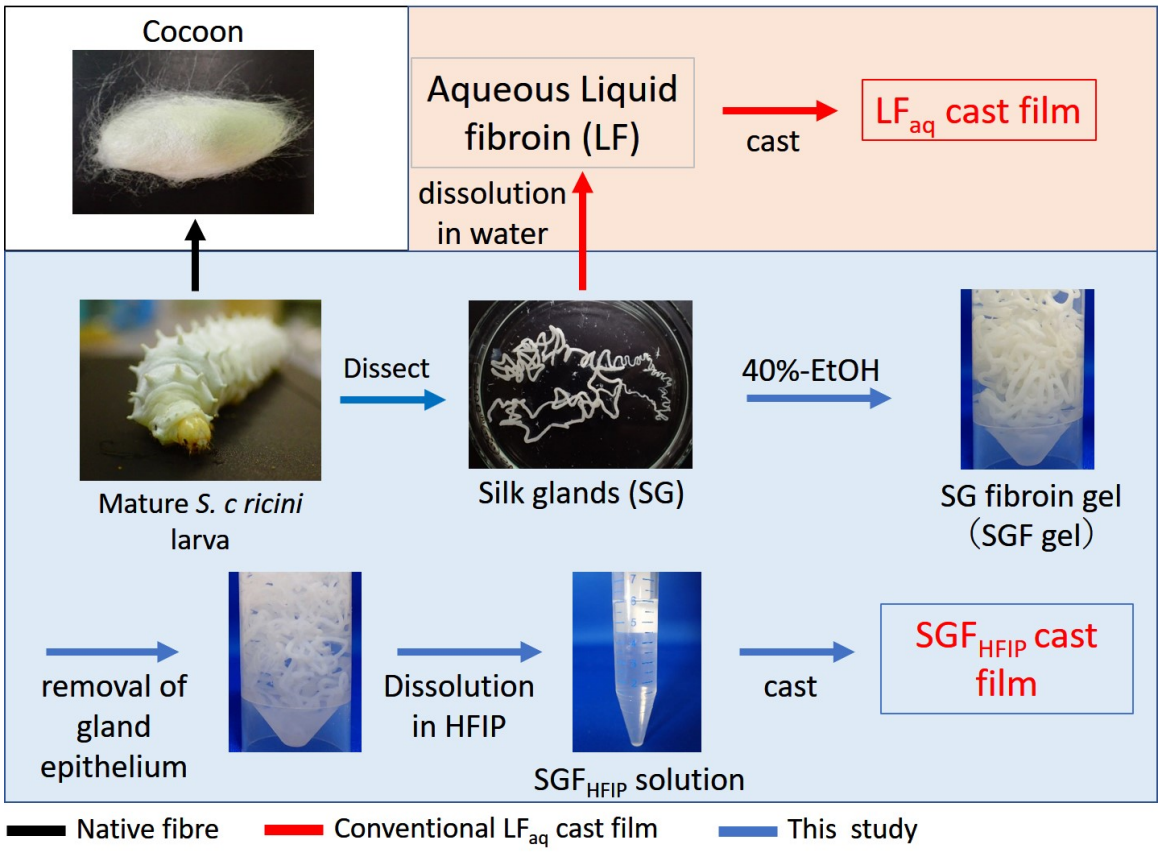


**Figure 1-1**

**A summary of the schemes used in the preparation of *S. c. ricini* native fibre (indicated by a black arrow), and films cast from aqueous liquid fibroin ($LF_{aq}$; indicated by red arrows) and 1,1,1,3,3,3-hexafluoro-2-propanol (HFIP) silk gland fibroin ($SGF_{HFIP}$; indicated by blue arrows) solutions.**

In this dissertation, characterization and controlled processing of *S. c. ricini* silk fibroin has been addressed. Conformational characterization to clarify the aggregation state of residual $\alpha$-helical domains and their influence on the mechanical properties of *S. c. ricini* native fibre is reported. As summarized in figure 1-1, three kinds of samples, native fibre, and films cast from aqueous liquid fibroin ($LF_{aq}$ cast film) and 1,1,1,3,3,3-hexafluoro-2-propanol (HFIP) silk gland fibroin ($SGF_{HFIP}$ cast film) solutions, were analysed. Consequently, insights gained from these

investigations were applied in controlled processing silk fibroin cast films for use as a biomaterial.

In Chapter II, "**Aggregation state of residual *α*-helices and their influence on the physical properties of *S. c. ricini* native fibre**", the residual *α*-helical domains were shown to be ordered, that is, they aggregate with a hexagonal packing, using X-ray scattering analyses. Further, the ordered aggregation size along the [10-10] lattice direction (32 Å) evaluated from the (10-10) peak width using the Scherrer equation is consistent with the small-angle scattering corresponding to a periodicity of 32.7 Å, suggesting long-range order of the aggregated *α*-helix bundles. The *α*-helix bundles transform to the *β*-sheet form at around 220 °C, accompanied by a substantial decrease of the characteristic plateau region in the stress-strain curve of the native fibre. Moreover, a direct connection between the plateau region and the *α*-helix to *β*-sheet structural transition was confirmed by X-ray scattering analyses before and after tensile stretching of a bundle of native fibre. These results suggest that the aggregated state of the residual *α*-helical domains is systematically and strategically designed by *S. c. ricini* silkworms to impart flexibility in the fibre.

With the understanding of the role of the *α*-helical domains in the fibre formation process and their influence on mechanical properties of native fibre, a mild strategy in was employed in the fabrication of *α*-helix-rich, and water insoluble film from a solution silk gland fibroin in HFIP without post-treatment in Chapter III; "s**tructure water-solubility relationship in *α*-helix-rich films cast from aqueous and 1,1,1,3,3,3-hexafluoro-2-propanol solutions of *S. c. ricini* silk fibroin**". The structural origin of the water-insolubility property is confirmed to be a small amount of *β*-sheet structure induced by ethanol treatment of the silk gland fibroin prior to dissolution in HFIP. In conformity with the results obtained in the preceding Chapter, the *α*-helical domains in the film aggregate with a hexagonal packing.

In-addition, the film can be uniaxially wet-drawn to a draw ratio of about three (3) to give highly oriented films.

Finally, the output of the current work and prospects for future research are given in Chapter IV, "**Concluding remarks**". It is noted that, the existence of the residual "$\alpha$-helical form" and small amount of $\beta$-sheet structure, influence the physical properties of *S. c. ricini* native fibre and the solubility in water of the film cast from a solution of fibroin in HFIP, respectively. Clearly, these are structure-property relationships. This knowledge is anticipated to form a basis for fruitful strategies in the design and development of amino acid sequences for artificial silks with desired properties. Besides expanding the options for biomaterial design, further studies to clarify the full utility of the novel $\alpha$-helix-rich silk fibroin film will be necessary.

**References**


[1] Craig, C. L. Evolution of arthropod silks. *Annu. Rev. Entomol.* **42**, 231–267 (1997).

[2] Yukuhiro, K., Sezutsu, H., & Yonemura, N. Evolutionary divergence of lepidopteran and trichopteran fibroins. In *Biotechnology of silk* (pp. 25-47). Springer, Dordrecht. (2014).

[3] Vollrath, F. & Porter, D. Silks as ancient models for modern polymers. *Polymer* **50**, 5623–5632 (2009).

[4] Fu, C., Shao, Z. & Fritz, V. Animal silks: their structures, properties and artificial production. *ChemComm* **43**, 6515 (2009).

[5] Porter, D. & Vollrath, F. Silk as a biomimetic ideal for structural polymers. *Adv. Mater.* **21**, 487–492 (2009).

[6] Sezutsu, H. & Yukuhiro, K. The complete nucleotide sequence of the Eri-silkworm (*Samia cynthia ricini*) fibroin gene. *J. Insect Biotechnol. Sericology* **83**, 59–70 (2014).

[7] Yukuhiro, K., Kanda, T. & Tamura, T. Preferential codon usage and two types of repetitive motifs in the fibroin gene of the Chinese oak silkworm, *Antheraea pernyi*. *Insect Mol. Biol*. **6**, 89–95 (1997).

[8] Sezutsu, H. & Yukuhiro, K. Dynamic rearrangement within the *Antheraea pernyi* silk fibroin gene is associated with four types of repetitive units. *J. Mol. Evol.* **51**, 329–338 (2000).

[9] Hwang, J., Lee, J., Goo, T., Yun, E., Lee, K., Kim, Y., Jin, B., Lee, S., Kim, K., Kang, S. & Suh, D. Cloning of the fibroin gene from the oak silkworm, *Antheraea yamamai* and its complete sequence. *Biotechnol. Lett.* **23**, 1321–1326 (2001).

[10] Gupta, A. K., Mita, K., Arunkumar, K. P. & Nagaraju, J. Molecular architecture of silk fibroin of Indian golden silkmoth, *Antheraea assama*. *Sci. Rep.* **5**, 12706 (2015).

[11] Datta, A., Ghosh, A. K. & Kundu, S. C. Purification and characterization of fibroin from the tropical Saturniid silkworm, *Antheraea mylitta*. *Insect Biochem. Mol. Biol.* **31**, 1013–1018 (2001).

[12] Zhou, C. Z., Confalonieri, F., Medina, N., Zivanovic, Y., Esnault, C., Yang, T., Jacquet, M., Janin, J., Duguet, M., Perasso, R. & Li, Z. G. Fine organization of *Bombyx mori* fibroin heavy chain gene. *Nucleic Acids Res*. **28**, 2413–2419 (2000).

[13] Sezutsu, H., Uchino, K., Kobayashi, I., Tamura, T. and Yukuhiro, K. Extensive sequence rearrangements and length polymorphism in fibroin genes in the wild silkmoth, *Antherea yamamai* (Lepidoptera, Saturniidae). *Int. J. Wild Silkmoth and Silk* **15**, 35-50 (2010).

[14] Zethner, O.; Koustrup, R.; Nguku, E.; Raina, S.K. *African ways of silk*, 2nd ed.; Regal Press Kenya Ltd.: Nairobi, Kenya (2017).

[15] Raina, S. K., Kioko, E., Zethner, O., & Wren, S. Forest habitat conservation in Africa using commercially important insects. *Ann. Rev. Entomol*. **56**, 465–485. (2011).

[16] Holland, C., Numata, K., Rnjak-Kovacina, J. & Seib, F. P. The biomedical use of silk: Past, present, future. *Adv. HealthC Mater.* **8**, 1800465 (2019).

[17] Rockwood, D. N., Preda, R. C., Yücel, T., Wang, X., Lovett, M. L. & Kaplan, D. L. Materials fabrication from *Bombyx mori* silk fibroin. *Nat. Protoc* **6**, 1612–1631 (2011).

[18] Langer, R. & Vacanti, J. P. Tissue engineering. *Science* **260**, 920–926 (1993).

[19] Borkner, C. B., Elsner, M. B. & Scheibel, T. Coatings and films made of silk proteins. *ACS Appl. Mater. Interfaces* **6**, 15611–15625 (2014).

[20] Silva, S. S., Oliveira, N. M., Oliveira, M. B., da Costa, D. P. S., Naskar, D., Mano, J. F., Kundu, S. C. & Reis, R. L. Fabrication and characterization of Eri silk fibres-based sponges for biomedical application. *Acta Biomater.* **32**, 178–189 (2016).

[21] Minoura, N., Aiba, S., Higuchi, M., Gotoh, Y., Tsukada, M. & Imai, Y. Attachment and growth of fibroblast cells on silk fibroin. *Biochem. Biophys. Res. Commun.* **208**, 511–516 (1995).

[22] Tanaka, C., Asano, A., Kurotsu, T. & Asakura, T. Structural study of silk-like peptides modified by the addition of the cell adhesive sequence, RGD, using $^{13}C$ CP/MAS NMR. *Polymer J.* **41**, 18–19 (2009).

[23] Bray, L., Suzuki, S., Harkin, D. & Chirila, T. Incorporation of exogenous RGD peptide and inter-species blending as strategies for enhancing human corneal limbal epithelial cell growth on *Bombyx mori* silk fibroin membranes. *J. Funct. Biomater.* **4**, 74 88 (2013).

[24] Tanaka, C. & Asakura, T. Synthesis and characterization of cell-adhesive silk-like proteins constructed from the sequences of Anaphe silk fibroin and fibronectin. *Biomacromolecules* **10**, 923–928 (2009).

[25] Oduor, E. O., Ciera, L., Adolkar, V., Pido, O. Eri silkworm rearing practices in Kenya. *J. Entomol. Zool. Stud.* **4**, 197-201 (2016).

[26] Dutta, S., Talukdar, B., Bharali, R., Rajkhowa, R. & Devi, D. Fabrication and characterization of biomaterial film from gland silk of Muga and Eri silkworms. *Biopolymers* **99**, 326–333 (2013).

[27] Magoshi, J., Magoshi, Y. & Nakamura, S. Mechanism of fibre formation of silkworm. In *Silk polymers*, ACS Symposium Series; American Chemical Society: Washington, D.C, WA, USA. Vol. 544, Chapter 25, 292–310 (1993).

[28] Yoshioka, T., Hata, T., Kojima, K., Nakazawa, Y. & Kameda, T. Fabrication scheme for obtaining transparent, flexible, and water-insoluble silk films from apparently dissolved silk-gland fibroin of *Bombyx mori* silkworm. *ACS Biomater. Sci. Eng.* **3**, 3207–3214 (2017).

[29] Spek, E. J., Olson, C. A., Shi, Z. & Kallenbach, N. R. Alanine is an intrinsic $\alpha$-helix stabilizing amino acid. *J. Am. Chem. Soc.* **121**, 5571–5572 (1999).

[30] Guo, C., Zhang, J., Jordan, J. S., Wang, X., Henning, R. W. & Yarger, J. L. Structural comparison of various silkworm silks: An insight into the structure–property relationship. *Biomacromolecules* **19**, 906–917 (2018).

[31] Fang, G., Sapru, S., Behera, S., Yao, J., Shao, Z., Kundu, S. C. & Chen, X. Exploration of the tight structural–mechanical relationship in mulberry and non-mulberry silkworm silks. *J. Mater. Chem. B* **4**, 4337–4347 (2016).

[32] Yang, M., Yao, J., Sonoyama, M. & Asakura, T. Spectroscopic characterization of heterogeneous structure of *Samia cynthia ricini* silk fibroin induced by stretching and molecular dynamics simulation. *Macromolecules* **37**, 3497–3504 (2004).

[33] Rousseau, M. E., Lefevre, T., Beaulieu, L., Asakura, T. & Pezolet, M. Study of protein conformation and orientation in silkworm and spider silk fibres using Raman microspectroscopy. *Biomacromolecules* **5**, 2247–2257 (2004).

[34] Rousseau, M. E., Beaulieu, L., Lefèvre, T., Paradis, J., Asakura, T. & Pèzolet, M. Characterization by Raman microspectroscopy of the strain-induced conformational transition in fibroin fibres from the silkworm *Samia cynthia ricini*. *Biomacromolecules* **7**, 2512–2521 (2006).

[35] Boulet-Audet, M., Vollrath, F. & Holland, C. Identification and classification of silks using infrared spectroscopy. *J. Exp. Biol.* **218**, 3138–3149 (2015).

[36] Nakazawa, Y. & Asakura, T. Structure determination of a peptide model of the repeated helical domain in *Samia cynthia ricini* silk fibroin before spinning by a combination of advanced solid-state NMR methods. *J. Am. Chem. Soc.* **125**, 7230–7237 (2003).

[37] Asakura, T., Nishimura, A., Kametani, S., Kawanishi, S., Aoki, A., Suzuki, F., Kaji, H. & Naito, A. Refined crystal structure of *Samia cynthia ricini* silk fibroin revealed by solid-state NMR investigations. *Biomacromolecules* **18**, 1965–1974 (2017).

[38] Tsukada, M., Freddi, G., Kasai, N. & Monti, P. Structure and molecular conformation of tussah silk fibroin films treated with water–methanol solutions: Dynamic mechanical and thermomechanical behavior. *J. Polym. Sci. Polym. Phys.* **36**, 2717–2724 (1998).

[39] Minoura, N., Tsukada, M. & Nagura, M. Physico-chemical properties of silk fibroin membrane as a biomaterial. *Biomaterials* **11**, 430–434 (1990).

[40] Rider, P., Zhang, Y., Tse, C., Zhang, Y., Jayawardane, D., Stringer, J., Callaghan, J., Brook, I. M., Miller, C. A., Zhao, X. & Smith, P. J. Biocompatible silk fibroin scaffold prepared by reactive inkjet printing. *J. Mater. Sci.* **51**, 8625–8630 (2016).

[41] Yoshioka, T., Tashiro, K. & Ohta, N. Molecular orientation enhancement of silk by the hot-stretching-induced transition from $\alpha$-helix-HFIP complex to $\beta$-sheet. *Biomacromolecules* **17**, 1437–1448 (2016).

[42] Drummy, L. F., Phillips, D. M., Stone, M. O., Farmer, B. L. & Naik, R. R. Thermally induced $\alpha$-helix to $\beta$-sheet transition in regenerated silk fibres and films. *Biomacromolecules* **6**, 3328–3333 (2005).

# Chapter II

## Aggregation State of Residual *α*-Helices and their Influence on the Physical Properties of *S. c. ricini* Native Fibre

### 2.1. Introduction

Towards establishing a sustainable society, effective utilization of *Saturniidae* wild-silkworm silks is receiving increased attention because of their excellent material properties, abundant yields in nature and promising applications [1]. As indicated chapter I, silk produced by the now semi-domesticated wild-silkworm, *S. c. ricini*, whose structure and mechanical properties have been well investigated, is one of the most promising candidates. It is one of the most studied among the silks obtained from non-mulberry sericulture [1,2]. Indeed, *S. c. ricini* silk fibroin is attracting increasing attention in diverse fields especially in the biomedical field as a source of biomaterials [3,4].

Earlier X-ray diffraction analyses classified *S. c. ricini* native fibre under group 3a, that is, they have a poly-L-alanine type *β*-sheet structure with an inter-sheet packing of 10.6 Å [5]. With the advancement of sequencing technology, the primary structure of *S. c. ricini* silk fibroin has been clarified to typically comprise of alternating repeat poly-L-alanine, $Ala_{(12\text{-}13)}$, and Gly-rich sequence regions [2]. In contrast, silk fibroin synthesized by the mulberry silkworm, *B. mori*, mainly consists of a $(GAGAGS)_n$ repeat sequence [6,7]. This characteristic assembly in the primary structure of *S. c. ricini* silk fibroin is almost similar to that of silks produced by other *Saturniidae* wild silkworms such as *A. pernyi* [8,9], *A. yamamai* [10], *A. assama* [11] and *A. mylitta* [12], as well as the major ampullate silk of spiders (although their poly-L-alanine sequences are shorter, $Ala_{(5\text{-}6)}$ [13,14]. Similar to the poly-L-alanine sequences in *S. c. ricini* and other native wild silk fibroins, X-ray diffraction, and infra-red, Raman and high resolution solid-state NMR spectroscopy studies [15-24] have shown the $(GAGAGS)_n$

repeat sequence regions in *B. mori* silk fibroin to dominantly contribute to the formation *β*-sheets [17,19-21,25,26]. In addition, the two kinds of silk fibroin have other conformations such as *α*-helix and random coil [21,27].

The heterogeneous nature of silk fibroin is believed to influence the fibre structure and mechanical performance of silks. Indeed, variability in the mechanical properties of various silks has been closely linked to the differences in primary, secondary and hierarchical structures of silk fibroin [21,28,29]. For instance, *B. mori* and *S. c. ricini* silks have *β*-sheet structures but exhibit distinct mechanical properties; *S. c. ricini* native fibres exhibit a characteristic plateau region in their stress-strain curve whereas *B. mori* native fibres exhibit a distinct yield point [21,28-30]. This unique feature, also observed in other wild silks [21,28,29], is often interpreted to be a result of some structural transitions, such as helical to zigzag conformations in poly(ethylene oxide) [31], *α*-helix to *β*-sheet structure in keratin [32,33], and amorphous to crystalline states in natural rubber [34]. Additionally, since the predominant feature in saturniid fibroin sequences is the highly repetitive alternating poly-L-alanine and Gly-rich regions, the phenomenon was also recently hypothesized to reflect coordinated molecular movement that may arise from the high degree of regularity in the amino acid sequences [29].

Studies on the structural formation of *S. c. ricini* silk have widely been performed using silk dope from the posterior silk glands of mature larvae. Based on $^{13}C$ solid-state NMR spectroscopy, films cast from water solutions of liquid fibroin have been clarified to have a *α*-helical conformation [22,35,36], the amino acid component in the *α*-helix domain being dominantly from the poly-L-alanine regions [37]. Moreover, structural transition from the *α*-helical conformation to the *β*-sheet structure during stretching of semi-dried *S. c. ricini* silk dope [16], considered to correspond to the natural spinning process [22], has been successfully traced by $^{13}C$ CP-MAS, X-ray diffraction and Raman spectroscopic analyses [16]. In addition, it has been verified that a small amount of the *α*-helical conformation remains during stretching

and even in the native fibre during the natural spinning process [38]. However, the aggregation state of the residual $\alpha$-helical domains, and their influence on the physical properties of the native fibre are yet to be clarified.

In this chapter the author aimed to; (a) confirm the presence of residual $\alpha$-helical domains in *S. c. ricini* native fibre, and (b) clarify their aggregation state, that is, if they are ordered or not, and their influence, if any, on the mechanical properties of the native fibre. To achieve this, detection of the presence of the residual $\alpha$-helical domains is imperative. Further evaluations would include clarification of whether they transform to the $\beta$-sheet structure during stretching, and if complete transformation of the residual $\alpha$-helices can be attained. If the structural transition occurs, then the effect on the physical properties of the fibre will be evaluated.

To achieve these, two kinds of samples were prepared as summarized in Figure 1-1 in chapter I. (1). Silk dope was obtained from the posterior silk glands of mature larvae (processing route indicated by red arrows) and diluted to give an aqueous solution of liquid fibroin from which cast films were prepared (herein referred to as $LF_{aq}$ as-cast films). (2). Native fibre were obtained from cocoons spun by larvae (processing route indicated by black arrow) from the same batch from which the silk dope was obtained. Detailed structural analyses of the silk samples were carried out by $^{13}C$ CP-MAS solid-state NMR spectroscopy, Fourier transform infra-red spectroscopy (FTIR), wide angle X-ray diffraction (WAXD) and differential scanning calorimetry (DSC).

## 2.2. Materials and Methods

### 2.2.1. Preparation of *S. c. ricini* $LF_{aq}$ As-Cast Film and Native Fibre

*S. c. ricini* silkworm larvae were reared in the laboratory on an all-instar artificial diet, SilkMate L4M (Nosan Corp., Yokohama, Japan) at 25 ± 3 °C and a relative humidity of 65 ± 3 %. Late fifth instar larvae, just after the gut purge, were sub-divided into two batches. The

first batch was anaesthized in ice for 15 min and dissected to obtain intact silk glands. The silk glands were briefly rinsed in ice cold Milli-Q water and silk dope in the lumen of the posterior silk glands was drained into cold Milli-Q water and carefully rinsed by exchanging the Milli-Q water several times to remove any contaminants. The thus-obtained silk dope was then diluted with Milli-Q water to give an aqueous solution of fibroin, herein referred to as liquid fibroin that was gently cast on polystyrene Petri-dishes. After drying at 23 ± 2 °C and a relative humidity of 30 ± 2% [39], transparent and flexible films ($LF_{aq}$ as-cast film) that could be peeled off the substrate with negligible mechanical damage were obtained. The thickness of the cast films was controlled by adjusting the concentration or volume of liquid fibroin cast. For comparison, the second batch of *S. c. ricini* larvae were let to spin cocoons at 25 ± 3 °C and a relative humidity of 65 ± 3 % whence native fibres analysed was obtained as described in the subsequent sub-Sections.

### 2.2.2. $^{13}C$ Cross Polarization – Magic Angle Spinning (CP/MAS) Solid-State NMR Spectroscopy

$^{13}C$ CP/MAS solid-state NMR measurements were performed with a Bruker Avance 600 WB (Karlsruhe, Germany) spectrometer with a magnetic field of 14.1 T at room temperature. The spectrometers were operated at a $^{13}C$ NMR frequency of 150.94 MHz. For each measurent, the fibroin protein sample was carefully cut into small pieces and packed into a solid-state probe and spun at a MAS frequency of 10.0 kHz in a 4.0 mm Ø zirconia rotor sample tube. A $^{1}H$ 90° pulse length of 3.5 $\mu$s and $^{1}H$-$^{13}C$ cross-polarization (CP) contact of 70 kHz were employed for the CP experiments. High-power $^{1}H$ decoupling using the SPINAL-64 method was employed. The repetition time for the CP experiments was 3.0 s and the $^{13}C$ chemical shifts were calibrated externally through the adamantane methylene peak at 29.5 ppm relative to tetramethyl silane, $(CH_3)_4Si$, (TMS) at 0 ppm. For native fibre, cocoon sections

analysed were sampled from the middle section of the middle layer of the cocoons obtained in sub-Section 2.2.1.

### 2.2.3. Fourier Transform Infra-red (FTIR) Spectroscopy

Since amide vibrations depend on the secondary structure of proteins, FTIR spectroscopy has been widely used in the study of the secondary structures of proteins. In the current study, FTIR measurements of the $LF_{aq}$ as-cast films were recorded at room temperature with an FTIR-620 (JASCO International Co. Ltd., Hachioji-shi, Japan) spectrometer in the transmission mode. For each measurement, 32 scans were co-added in the spectral range 4000 to 400 $cm^{-1}$ with a 2 $cm^{-1}$ resolution. The resultant spectrum was corrected by subtracting a background spectrum recorded under similar scan conditions. The assignments of conformation sensitive bands for *S. c. ricini* silk fibroin used in this report were: ~1625 and ~1519 $cm^{-1}$ as $\beta$-sheet structure [21,40] and ~1658 and 1545 - 1548 $cm^{-1}$ as $\alpha$-helix [4,40].

### 2.2.4. Wide-Angle X-Ray Diffraction Analyses

To clarify the aggregation state of the $\alpha$-helical domains in the $LF_{aq}$ as-cast film and native fibre, WAXD measurements were carried out with a 3.5 m NANOPIX X-ray diffractometer (Rigaku Corp., Tokyo, Japan) (40 kV, 30 mA, CuKα 1.5418 Å radiation) equipped with a highly sensitive single-photon counting pixel HyPix-6000 2D detector with a pixel size of 100 × 100 $\mu m^2$ (Rigaku Corp., Tokyo, Japan) as earlier described [41]. Calibration of the camera distance was carried out using cerium oxide powder and a background diffraction pattern collected under conditions similar to those used for sample analysis was subtracted from each measurement. Subtraction of air-scattering and extraction of $2\theta$-profiles from the 2-dimensional WAXD patterns obtained was done using a free software FIT2D, developed by A. P. Hammersley of the European Synchrotron Radiation Facility (Grenoble). The inter-planar

spacings (distance between the repeating units; *d*-spacing) were evaluated using Bragg's equation (equation 1);

$$n\lambda = 2d \sin \Theta \quad (1)$$

where *n* is an integer, which is the order of the reflection, λ is the wavelength of the incident radiation (CuKα 1.5418 Å radiation), and θ is the incident angle (angle between the incident ray and the scattering plane), whereas the crystallite size (D) along the [10-10] lattice direction was evaluated using Scherrer's equation (equation 2);

$$D = K\lambda / (\beta \cos \Theta) \quad (2)$$

where K is a dimensionless shape factor (Scherrer factor), λ is the wavelength of the incident X-ray beam (CuKα 1.5418 Å radiation), β is the full width at a half the maximum intensity (FWHM) of the (10-10) peak, and 2θ is the diffraction angle of the (10-10) peak. The FWHM (β) was corrected for instrumental peak broadening effect using the equation (equation 3);

$$\beta^2 = \beta^2_{obs} - \beta^2_{Al} \quad (3)$$

where $\beta_{obs}$ was the observed FWHM and $\beta_{Al}$ was FWHM observed for a sample of aluminum powder [42]. A value of 0.9, often used in the evaluation of the crystallite size of silkworm silk [43], was used for the shape factor, K.

To obtain the WAXD 2$\theta$-profile of liquid fibroin, an aliquot of the solution was rapidly frozen to -80 °C in an ultra-low temperature Nihon freezer (NF-10SF3, Tokyo, Japan) and lyophilized in an EYELA vacuum freeze-dryer (FDU 830, Tokyo, Japan) for 24 h. For heat-treated $LF_{aq}$ as-cast film and native fibre (sampled from the middle layer of the middle section of the cocoons obtained in sub-section 2.2.1), the samples were cut into small pieces each about 0.5 × 0.5 mm and separately sand-withched between thin glass slides (~1.0 mm thick),

alongside a thin and sensitive thermocouple to monitor the sample temperature directly. These were set on a digital hot-plate (Corning PC-420D), heated to 220 °C and kept at this temperature (annealed) for about 1 min and allowed to cool to room temperature.

### 2.2.5. Thermal Analyses

Differential scanning calorimetry (DSC) measurements were performed with a DSC Q200 analysis system (TA Instruments, New Castle, DE, USA). Instrument calibration for heat flow and temperature were done using indium, whereas for heat capacity, aluminum and sapphire were used. For each measurement, about 5.0 mg of the fibroin protein sample was encapsulated in an aluminum pan and heated between -30 and 430 °C at 2 °C $min^{-1}$ under a dry nitrogen gas flow of 50 mL $min^{-1}$.

The concentrations of liquid fibroin, and the weight loss profiles of the $LF_{aq}$ as-cast film and native fibre were determined by thermal gravimetry (TG) with a Thermoplus TG 8120 system (Rigaku Corp., Tokyo, Japan). For each measurement, about 1.0 mg of the fibroin protein was heated in an aluminium pan from room temperature to 430 °C at a heating rate of 2 °C $min^{-1}$ under a dry nitrogen gas flow of 200 ml $min^{-1}$.

### 2.2.6. Tensile Tests

Tensile properties of single fibres of *S. c. ricini* silk were measured in the dry state at 23 ± 2 °C and a relative humidity of 37 ± 2 %, with an EZ Test/CE mechanical tensile stage (Shimadzu Co., Kyoto, Japan) equipped with a 5 N load cell.

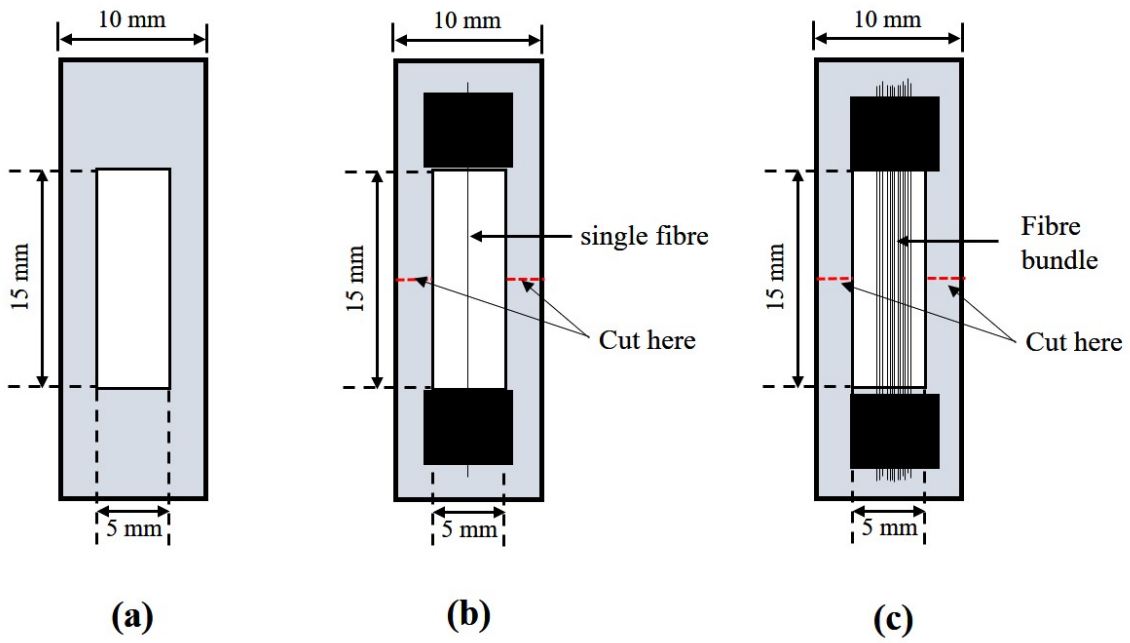


**Figure 2-1**

**A schematic diagram of a handmade paper frame (a) used as supports for single (b) and fiber bundle (c) of *S. c. ricini* fibre during the tensile tests.**

Single fibres, each approximately 6.0 cm, were carefully unravelled from the middle section of the middle layer of the native cocoons obtained in sub-section 3.1, sub-divided and labelled systematically (say A and B, for native and heat-treated tests, respectively). One set of the fibres were set using a kapton tape and sand-witched between thin glass slides (~1.0 mm thick), alongside a thin and sensitive thermocouple and heat-treated as described in chapter II. Each fibre (native and heat-treated) was then mounted without pre-load onto a rectangular handmade paper frame with an initial gauge length of 15 mm using glue (Figure 2-1a). After positioning the paper frame holding the test fibre on the tensile stage, both sides of the paper frame were gently cut as shown in figure 2-1b, and the tensile deformation behaviour was evaluated at a crosshead speed of 2 mm $min^{-1}$. The tensile properties reported were averaged from three measurements, each for native and heat-treated fibre. A paired *t*-test using

GraphPadPrism 5 (GraphPad Software, Inc., San Diego, CA, USA) was used to compare native and heat-treated data at 95% confidence interval., and then the measurement was started.

### 2.2.7. Strain-dependent structure transformation monitored by WAXD

To monitor structural changes in *S. c. ricini* native fibre during tensile deformation, a parallel-aligned bundle (shown in figure 2-1c), with a thickness of about 0.5 mm, was carefully prepared from single fibres obtained from the cocoons as already described [41]. The fibre bundle was fixed on a mechanical tensile stage (Linkam Scientific Instruments, Epsom, Tadworth, UK) with a 3.0 mm Ø hole for the X-ray beam to pass through. The micro-stretcher was equipped with a 10 N load cell and coupled to the 3.5 m NANOPIX X-ray diffractometer (Rigaku Corp., Tokyo, Japan) (see sub-section 2.2.4). The gauge distance was 20 mm and tensile deformation of the fibre bundle was carried out at a cross-head speed of 2 $\mu$m $sec^{-1}$. WAXD measurements were carried out at three stages, that is, before stretching, just after the plateau region, and after the fibre bundle breaks. The duration of exposure for each WAXD measurement was 30 min.

## 2.3. Results and Discussion

### 2.3.1. Ordered *α*-Helix Structure in *S. c. ricini* Liquid Fibroin As-Cast Film

Silk dope collected from the posterior silk glands of mature larvae of *S. c. ricini* was diluted with milli-Q water to give a transparent solution of liquid fibroin. Films cast from this solution ($LF_{aq}$ as-cast films) at 23 ± 2 °C and a relative humidity of 30 ± 2%, were transparent and flexible. The secondary structure of biopolymers obtained over a broad spectral range may be handy in understanding and predicting their properties and potential applications [44]. However, in this chapter the author focuses on the aggregation state of the $\alpha$-helical domains in the $LF_{aq}$ as-cast film, and clarification of some spectral features in the $LF_{aq}$ as-cast films will be discussed in chapter III. $^{13}C$ CP-MAS NMR spectra of the $LF_{aq}$ as-cast film and native fibre

were as shown in figure 2-2. The chemical shift assignments for the Ala $C_\beta$, Gly $C_\alpha$, Ala $C_\alpha$ and C=O spectral regions used in the current report are indicated in the spectra [16,21,24]. The native silk fibre was *β*-sheet-rich whereas the $LF_{aq}$ as-cast film was *α*-helix-rich. These results are consistent with previous work [12,22], and with our expectations since *S. c. ricini* liquid fibroin is known to have a well-structured *α*-helical conformation in the poly-L-alanine region [27]. This was well supported by FTIR as shown in the typically *α*-helix-rich FTIR spectrum of the $LF_{aq}$ as-cast film in figure 2-3. The amide I region of the spectrum is assigned to the *α*-helical conformation whereas the amide II region seems to contain a small amount of *β*-sheet or other components.

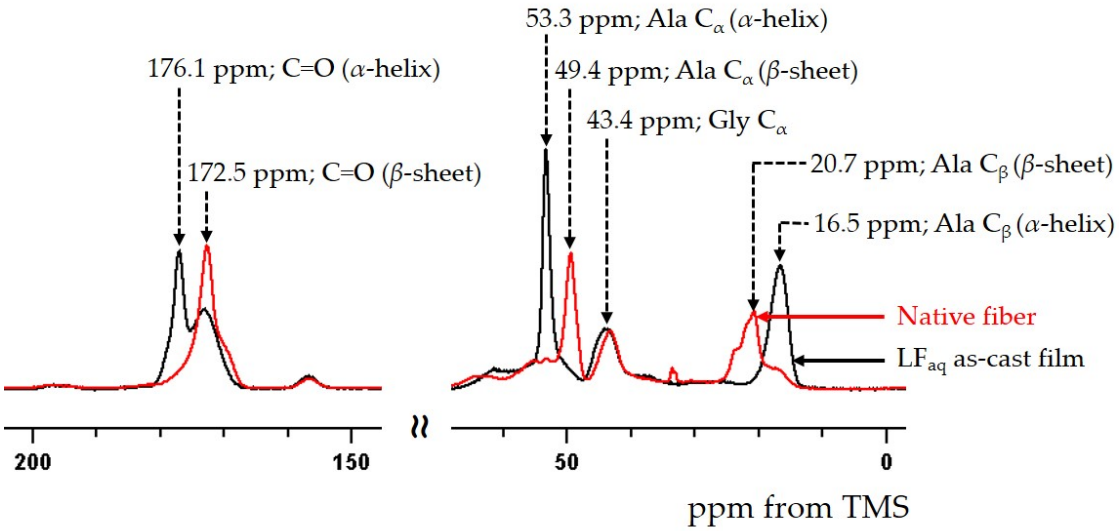


**Figure 2-2**

**$^{13}C$ CP-MAS solid-state NMR spectra of *S. c. ricini* $LF_{aq}$ as-cast film (spectrum in black) and native silk fibre (spectrum in red) from 0 to 60, and 150 to 200 ppm.**

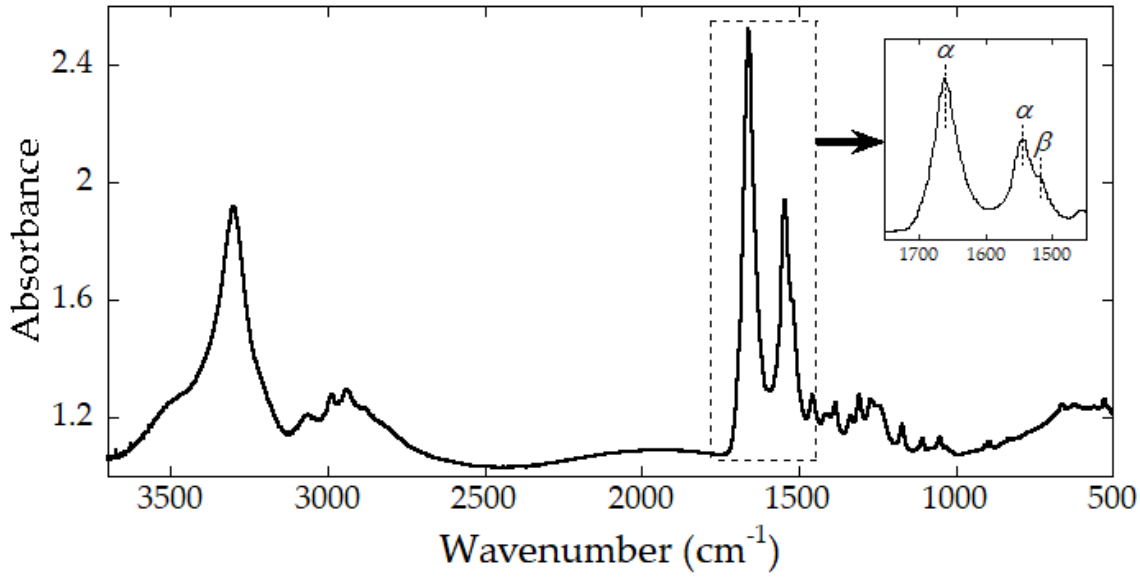


**Figure 2-3**

**A representative FTIR spectrum of *S. c. ricini* $LF_{aq}$ as-cast film. Inset is the spectrum showing the vibrational bands in the amide I and II regions.**

A WAXD $2\theta$-profile of the $LF_{aq}$ as-cast film is shown in figure 2-4. A strong and sharp peak at $2\theta = 11.6°$ (corresponding to $d = 7.6$ Å), a broad peak having an undefined peak-top at around $2\theta = 22.7°$ (corresponding to $d = 3.9$ Å) as well as a distinct small-angle scattering peak at $2\theta = 2.7°$ (corresponding to $d = 32.7$ Å) were detected. Similar peak combinations of the former two were observed for semi-dried *S. c. ricini* [16] and *A. pernyi* [35,36] silk dopes, and assigned to the $\alpha$-helix conformation. Based on X-ray structural analysis of a highly oriented crystalline $\alpha$-helix sample of poly-L-alanine, Bamford et al. determined a hexagonal unit cell ($a = 8.55$ Å), giving a strong diffraction of (10-10) plane at $d_{10\text{-}10} = 7.40$ Å [45]. A slightly lager $d$-spacing of (10-10) plane indicates a slightly larger hexagonal unit cell dimension, probably due to side chains of amino acid residues neighboring the poly-L-alanine sequence regions. The unclear broad peak at around 3.9 Å as well as the other similar observation in the abovementioned work on semi-dried *S. c. ricini* and *A. pernyi* silk dopes strongly suggest that the $\alpha$-helical domains (see figure 2-4a) aggregate with a hexagonal packing (see figure 2-4b),

but not perfectly crystallized as observed in poly-L-alanine [45] and poly-$\gamma$-methyl-L-glutamate [46]. The ordered aggregation size along the [10-10] lattice direction (roughly corresponding to the diameter of the cross-sectional area of the aggregated $\alpha$-helices bundle) was evaluated from the peak width of the (10-10) peak using the Scherrer equation to be 32 Å. This dimension is well consistent with the small-angle scattering corresponding to a periodicity of 32.7 Å, suggesting that the aggregated $\alpha$-helices bundles further form a hierarchical super-array with a neighboring distance of around 32-33 Å.

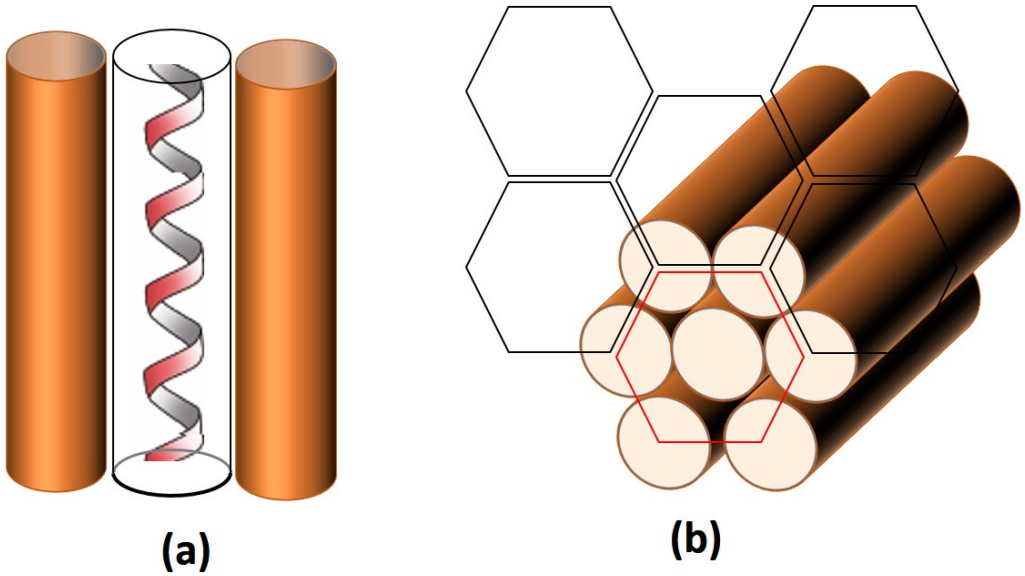


**Figure 2-4**

**Schematic representations of the α-helical domains (a) and the hexagonal packing of the α-helix bundles deduced.**

From the X-ray analyses, it is evident that the fibroin molecules in the $LF_{aq}$ as-cast film assemble into an ordered aggregated structure. To clarify the stage during which structural formation of the ordered $\alpha$-helices occurs, WAXD analysis of a freeze-dried sample, frozen at -80 °C, of the same liquid fibroin solution from which the $LF_{aq}$ film was cast, was performed. The WAXD $2\theta$-profile of the freeze-dried fibroin sample, shown in figure 2-5, was essentially

similar to that of the $LF_{aq}$ as-cast film. Considering previous work showing successful immobilization of the structure of silk fibroin by freezing at -80 °C [47,48], our experimental result strongly indicates the existence of the ordered aggregated structure in the aqueous state. This is consistent with a common consensus in natural spinning of spider [49] and *B. mori* silkworm [39] silks, in which liquid fibroin comes out of the spinneret in a liquid crystalline or nematic state. The formation of ordered aggregation in the $\alpha$-helical domains in the solution state of *S. c. ricini* seems quite reasonable to achieve efficient natural spinning, during which highly oriented and crystalline fibre is produced with consumption of minimum energy.

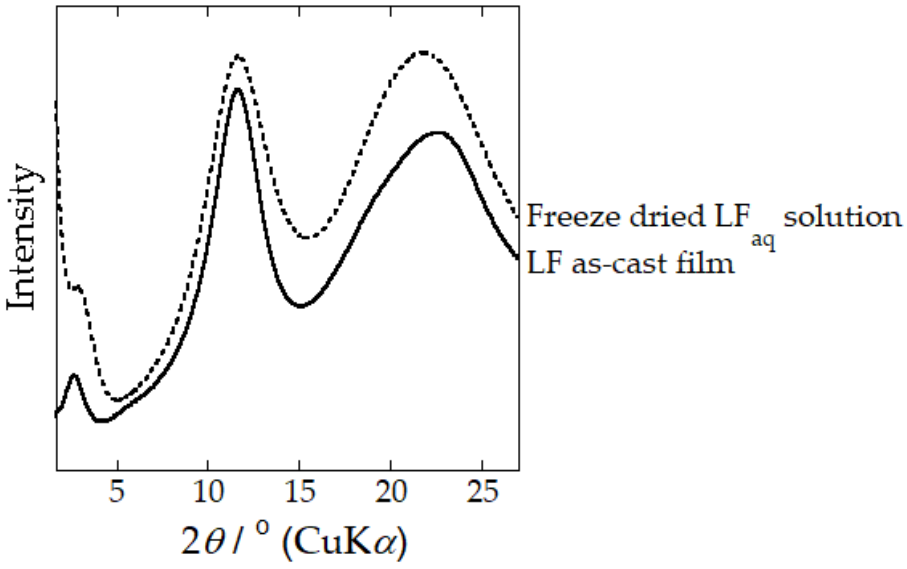


**Figure 2-5**

**WAXD 2$\theta$-profiles obtained for *S. c. ricini* $LF_{aq}$ as-cast film (solid line profile) and a freeze-dried sample of the liquid fibroin solution from which the film was cast (dotted line profile).**

Figure 2-6 shows the TG and DSC profiles of the $LF_{aq}$ as-cast film, and native and heat-treated *S. c. ricini* silk fibre. As seen in figure 2-6a,d a remarkably sharp exothermic peak, speculated to correspond to a structural transition from the ordered aggregated $\alpha$-helical conformation to the $\beta$-sheet structure, was detected at ~220 °C in the DSC profile of the $LF_{aq}$

as-cast film. To clarify the kind of transition that occurs, as cast and heat-treated (220°C, 1 min) $LF_{aq}$ films were subjected to WAXD analysis. WAXD 2$\theta$-profiles of native fibres (same profile shown in figure 2-5), and the as-cast and heat-treated $LF_{aq}$ film are shown in figure 2-7. A clear transition from the ordered aggregated $\alpha$-helix to $\beta$-sheet structure, induced by heat treatment, was confirmed. Such a narrow temperature window in the structural transition in the $LF_{aq}$ as-cast film (figure 2-6a,d) is considered to result from instantaneous solid-to-solid phase transition from the hexagonally packed $\alpha$-helix to the $\beta$-sheet structure with minimum molecular movement.

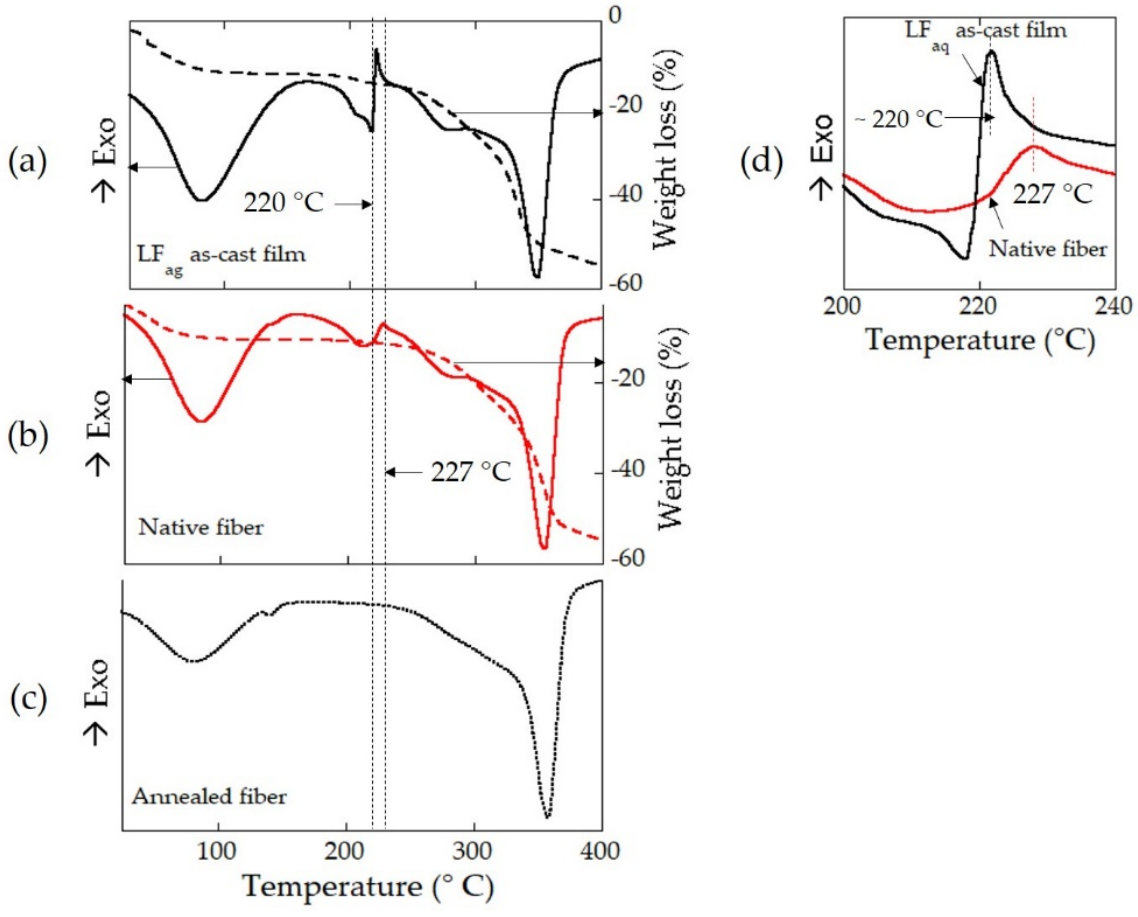


**Figure 2-6**

**TG and DSC profiles of *S. c. ricini* $LF_{aq}$ as-cast film (a), and native (b), and heat-treated (220 °C, 1 min; c) fibres. Panel d shows a comparison of the $LF_{aq}$ as-cast film (profile in black) and native silk fibre (profile in red) DSC profiles between 200 and 240 °C.**

### 2.3.2. Ordered *α*-Helix Structure in *S. c. ricini* Native Fibre

Although the WAXD *β*-sheet profile of the heat-treated $LF_{aq}$ cast film was essentially similar to that of the typically *β*-sheet-rich *S. c. ricini* native fibre (figure 2-7), a small but highly reproducible difference existed: A shoulder peak in the native fibre profile (indicated by the dotted red line) corresponding to the peak assigned to the ordered aggregated *α*-helix structure in the $LF_{aq}$ as-cast film in the preceding section was detected. We speculated the peak to indicate the presence of a small amount of residual ordered aggregated *α*-helix structure in the native fibre. This speculation was supported by the DSC results of native fibre in which a peak similar to the characteristic sharp exothermic peak in the DSC profile of $LF_{aq}$ as-cast film was detected (figure 2-6b). However, in the DSC profile of native fibre, the exothermic peak was broad, and with a slightly higher peak top temperature (~227 °C). Moreover, the endothermic peak is reversed, that is, it appears at a slightly lower temperature (figure 2-6d).

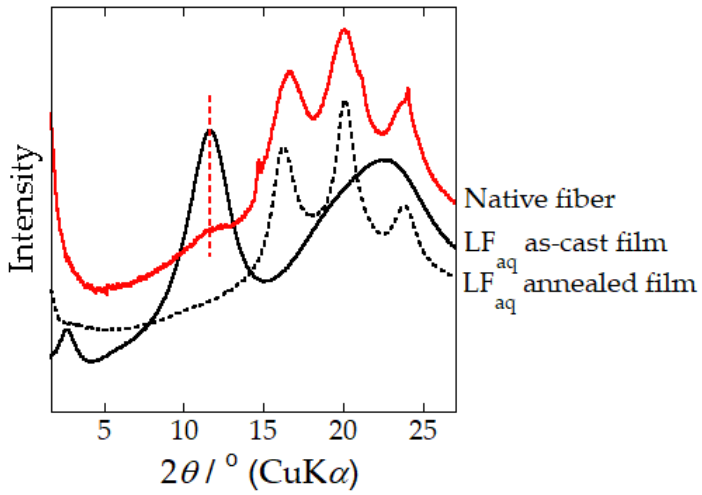


**Figure 2-7**

**WAXD 2$\theta$-profiles of native *S. c. ricini* silk fibre (profile in red), and as-cast (profile in black solid line) and heat-treated (220 °C, 1 min; profile in black dotted line) $LF_{aq}$ cast films.**

To account for the residual ordered $\alpha$-helices detected in the native fibre, it is considered that aggregated $\alpha$-helical domains with higher ordering preferentially transform to the $\beta$-sheet structure during natural spinning, whereas those with lower ordering are untransformed. In other words, the ordered aggregated $\alpha$-helix conformation in the native fibre is considered to be partially collapsed and has a slightly unstable structure. Hence, the structural transition (endothermic reaction) starts at a slightly lower temperature in the fibre than in the as-cast film. Often, the $\beta$-sheet structure is difficult to form, hence, subsequent $\beta$-sheet formation does not occur until a higher temperature is attained. For instance, in the assembled portion of amino acids where side chains are bulky, larger molecular motion (higher energy) is required because they hinder $\beta$-sheet formation, hence the exothermic peak occurs at a higher temperature. This implies that, sites where $\beta$-sheet formation is relatively difficult, that are untransformed during native spinning, exist in the ordered aggregated $\alpha$-helix structure. Further, the partial collapse of the originally ordered structure that results in broadening of the transition peak in the native fibre is considered to result from stretching and compression during spinning. The presence of the structure that does not easily transform to $\beta$-sheet may be considered intentional and a strategy of the *S. c. ricini* silkworms to impart flexibility in the silk.

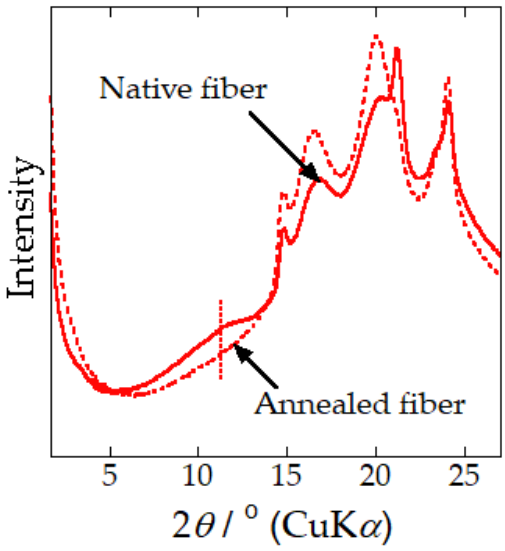


**Figure 2-8**

**WAXD 2$\theta$-profiles of native (profile in red solid line) and heat-treated (220 °C, 1 min; profile in red dotted line) *S. c. ricini* fibres.**

To clarify if the peak could not be ascribed to $\beta$-sheet but the ordered aggregated $\alpha$-helix structure, native fibres were heat-treated, under similar conditions described for the $LF_{aq}$ as-cast film and subjected to WAXD and DSC analyses. WAXD 2$\theta$-profiles of native (same profile shown in figure 2-7) and heat-treated silk fibres are shown in figure 2-8. Consistent with our earlier results for the heat-treated $LF_{aq}$ film, the peak disappeared accompanied by enhancement of the intensity of the peaks assigned to $\beta$-sheet structure. Similar disappearance of the exothermic peak in the DSC profile for heat-treated fibres was detected as shown in figure 2-6c). These results confirm that, though low in abundance, *S. c. ricini* native fibre contains an ordered aggregated $\alpha$-helix structure.

### 2.3.3. Impact of Heat-Treatment on the Mechanical Properties of Single *S. c. ricini* Native Fibre

In the preceding section, the author successfully detected a signal peak of residual ordered aggregation of $\alpha$-helices in the WAXD pattern of *S. c. ricini* native fibre. The residual

helices were confirmed to transform into $\beta$-sheet due to heat-treatment at around 220 °C by WAXD and DSC. Moreover, it is well established that stretching induces $\alpha$-helix to $\beta$-sheet structural transition in various types of silks such as regenerated *B. mori* silk [42], and spider [50], as well as *S. c. ricini* liquid fibroin-based materials [16,18]. However, the relationship between this structural transition and the characteristic plateau deformation behaviour in the stress-strain curve of *S. c. ricini* native fibre remains unclear. To clarify the relationship, the effect of heat-treatment on the plateau phase in the stress-strain curve of single *S. c. ricini* native fibres was investigated. The cross-sectional areas of native silk fibre have been shown to vary along the silk fibre axis [29], due to flaws possibly associated with the larvae's spinning behavior [51] often affected by among other factors, temperature and relative humidity [52]. Hence, since the cross-sectional areas of the individual test fibres were not evaluated in the current study, fibre sampled from adjacent portions of single fibre carefully unraveled from the from the middle layer of the middle part of the cocoon were used for the tensile tests before and after heat-treatment, respectively, to reduce variability. Therefore, the mechanical properties discussed here are an estimation from the representative force (N) against strain (%) plots. Further, the heat-treatment temperature was chosen based on the DSC data discussed in preceding section, where $\alpha$ to $\beta$-sheet structural transition was confirmed, under a similar heat-treatment regime for native fibre (cocoon sections) used for WAXD analyses. The results of the tensile tests of native and heat-treated *S. c. ricini* silk single fibres were reproducible, and representative stress-strain curves were as shown in figure 2-9.

A distinct plateau region was detected in the stress-strain curve of native silk fibre but was absent or significantly diminished in the stress-strain curve of the heat-treated fibre. Further, the stress-strain curve of the heat-treated single fibres transformed to be like that of *B. mori* and exhibited a lower strain to break (extensibility). The disappearance of the plateau phase and lower extensibility were speculated to be due to $\alpha$ to $\beta$-sheet structural transition,

caused by the heat-treatment (see figure 2-9), already clarified in the preceding section. This is because heat-treatment reduces the residual $\alpha$-helical chains (increases the $\beta$-sheet content) in the fibres which often results in enhanced stiffness [53]. In the current study, the fibre spinning process has been shown to play a key role in determining the unique material properties of *S. c. ricini* native fibres, in addition to the highly repetitive silk fibroin protein amino acid sequence in various silks recently reported by Malay et al. [29].

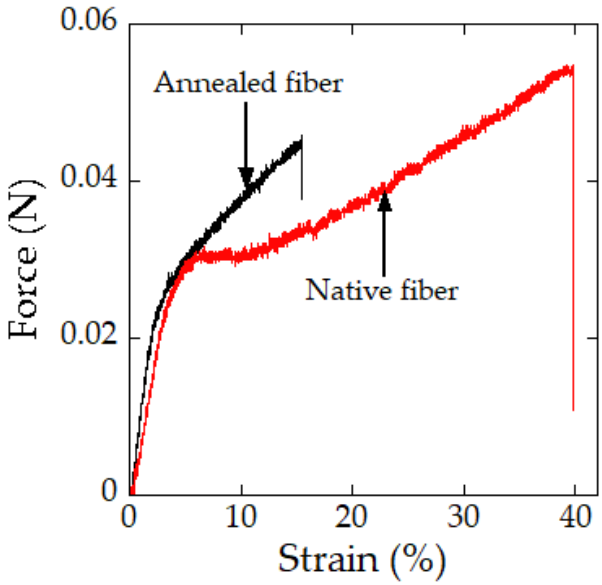


**Figure 2-9**

**Representative force-strain curves of native (curve in red), and heat-treated (220 °C, 1 min; curve in black) *S. c. ricini* single silk fibres.**

### 2.3.4. Strain-Induced $\alpha$-Helix to $\beta$-sheet transition in *S. c. ricini* native fibre traced by WAXD

To investigate the relationship between the plateau deformation behavior and the residual $\alpha$-helix to $\beta$-sheet structural transition, WAXD measurements of a parallel-aligned bundle of *S. c. ricini* native fibres were performed at three different stages; before stretching (intact fibre-bundle; ①), just after the plateau region ③, and after fibre bundle breaks ⑥. As

depicted in figure 2-10a, stretching was paused just after the plateau region, corresponding to $\varepsilon$ = 16 % (indicated by arrow ②). This was immediately followed by a rapid drop in force, corresponding to stress relaxation, as seen beyond point ②. The second WAXD measurement was started after the stress relaxation was almost saturated as indicated by arrow ③. Due to inter-strand hydrogen bonding, $\beta$-sheets are energetically favorable, that is, they are high-temperature relaxed structures [54] and the structural transition from $\alpha$-helix to $\beta$-sheet is irreversible. Hence, the influence of stress relaxation on the purpose of this WAXD measurement, that is, to trace the changes of the signal peak of ordered aggregation of $\alpha$-helices, was considered negligible.

After the second WAXD measurement, the fibre bundle was again stretched (indicated by arrow ④) until break (indicated by arrows ⑤ and ⑥). This was followed by a third WAXD measurement ⑥, without distorting the broken but parallel-aligned fibre bundle on the Linkam micro-stretcher. The equatorial $2\theta$-profiles scanned from the resultant WAXD patterns were as shown in figure 2-10b. In addition to the equatorial (020) and (210) $\beta$-sheet reflections, the signal reflection of the (10-10) ordered residual $\alpha$-helices was clearly detected in the intact native fibre. This peak was observed to decrease gradually with increasing strain. A significant decrease in the peak intensity of this signal reflection was observed after the fibre bundle broke; however, the decrease majorly occurred before the end of the plateau region. This observation suggests $\beta$-sheet formation to occur at the expense of the $\alpha$-helix structure.

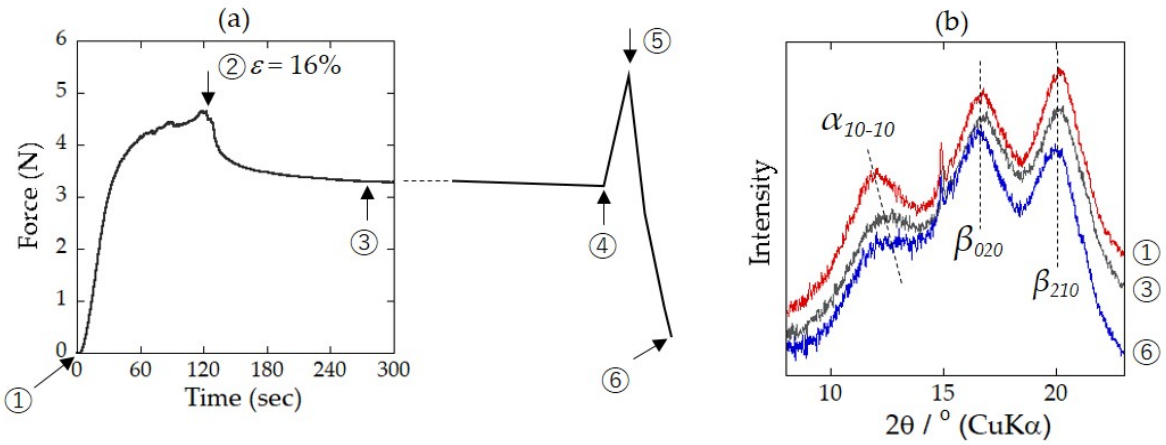


**Figure 2-10**

**(a) Force-time curve, and (b) WAXD 2$\theta$-profiles of a parallel-aligned bundle of *S. c. ricini* native fibre before stretching ① (profile in red), just after the plateau region ($\varepsilon$ = 16 %; ③; profile in black), and after the fibre bundle broke ⑥ (profile in blue).**

### 2.4. Conclusions

In this chapter, the presence of a small amount of $\alpha$-helical conformation that is untransformed during the natural spinning process (herein referred to as residual $\alpha$-helical conformation) was confirmed by X-ray scattering and thermal analyses. X-ray scattering analyses revealed that the residual $\alpha$-helical domains are ordered, that is, they aggregate in a hexagonal packing. Moreover, the ordered aggregation size along the [10-10] lattice direction (32 Å) evaluated from the full width at half maximum of the (10-10) peak using the Scherrer equation was consistent with the small-angle scattering corresponding to a periodicity of 32.7 Å. This suggested that the aggregated $\alpha$-helical bundles further form a hierarchical super-array with a neighboring distance of between 32–33 Å. When stretched, subjected to heat (~220 °C) or ethanol, the ordered aggregated $\alpha$-helical domains transform to the $\beta$-sheet structure, accompanied by a substantial decrease or diminishing of the characteristic plateau region in the stress-strain curve of native fibre. WAXD results obtained before and after stretching of a bundle of native fibre demonstrated a direct connection between the characteristic plateau

phase and the structural transition from the ordered aggregated residual $\alpha$-helical domains to the $\beta$-sheet structure. These results suggest that the aggregated state of the residual $\alpha$-helical domains is systematically and strategically designed by *S. c. ricini* silkworms to impart flexibility in the fibre.

**References**


[1] Zethner, O.; Koustrup, R.; Nguku, E.; Raina, S.K. *African ways of silk*, 2nd ed.; Regal Press Kenya Ltd.: Nairobi, Kenya (2017).

[2] Sezutsu, H. & Yukuhiro, K. The complete nucleotide sequence of the Eri-silkworm (*Samia cynthia ricini*) fibroin gene. *J. Insect Biotechnol. Sericology* **83**, 59–70 (2014).

[3] Silva, S. S., Oliveira, N. M., Oliveira, M. B., da Costa, D. P. S., Naskar, D., Mano, J. F., Kundu, S. C. & Reis, R. L. Fabrication and characterization of Eri silk fibres-based sponges for biomedical application. *Acta Biomater.* **32**, 178–189 (2016).

[4] Dutta, S., Talukdar, B., Bharali, R., Rajkhowa, R. & Devi, D. Fabrication and characterization of biomaterial film from gland silk of Muga and Eri silkworms. *Biopolymers* **99**, 326–333 (2013).

[5] Warwicker, J. O. Comparative studies of fibroins: II. The crystal structures of various fibroins. *J. Mol. Biol.* **2**, 350–362 (1960).

[6] Zhou, C. Z., Confalonieri, F., Medina, N., Zivanovic, Y., Esnault, C., Yang, T., Jacquet, M., Janin, J., Duguet, M., Perasso, R. & Li, Z. G. Fine organization of *Bombyx mori* fibroin heavy chain gene. *Nucleic Acids Res*. **28**, 2413–2419 (2000).

[7] Zhou, C. Z., Confalonieri, F., Jacquet, M., Perasso, R., Li, Z. G. & Janin, J. Silk fibroin: Structural implications of a remarkable amino acid sequence. *Proteins* **44**, 119–122 (2001).

[8] Yukuhiro, K., Kanda, T. & Tamura, T. Preferential codon usage and two types of repetitive motifs in the fibroin gene of the Chinese oak silkworm, *Antheraea pernyi*. *Insect Mol. Biol*. **6**, 89–95 (1997).

[9] Sezutsu, H. & Yukuhiro, K. Dynamic rearrangement within the *Antheraea pernyi* silk fibroin gene is associated with four types of repetitive units. *J. Mol. Evol.* **51**, 329–338 (2000).

[10] Hwang, J., Lee, J., Goo, T., Yun, E., Lee, K., Kim, Y., Jin, B., Lee, S., Kim, K., Kang, S. & Suh, D. Cloning of the fibroin gene from the oak silkworm, *Antheraea yamamai* and its complete sequence. *Biotechnol. Lett.* **23**, 1321–1326 (2001).

[11] Gupta, A. K., Mita, K., Arunkumar, K. P. & Nagaraju, J. Molecular architecture of silk fibroin of Indian golden silkmoth, *Antheraea assama*. *Sci. Rep.* **5**, 12706 (2015).

[12] Datta, A., Ghosh, A. K. & Kundu, S. C. Purification and characterization of fibroin from the tropical Saturniid silkworm, *Antheraea mylitta*. *Insect Biochem. Mol. Biol.* **31**, 1013–1018 (2001).

[13] Hinman, M. B. & Lewis, V. R. Isolation of a clone encoding a second dragline silk fibroin. *J. Biol. Chem*. **267**, 19320–19324 (1992).

[14] Gosline, J. M., Guerette, P. A., Ortlepp, C. S. & Savage, K. N. The mechanical design of spider silks: From fibroin sequence to mechanical function. *J. Exp. Biol.* **202**, 3295–3303 (1999).

[15] Arnott, S., Dover, S. D. & Elliott, A. Structure of $\beta$-poly-L-alanine: Refined atomic co-ordinates for an anti-parallel beta-pleated sheet. *J. Mol. Biol*. **30**, 201–208 (1967).

[16] Yang, M., Yao, J., Sonoyama, M. & Asakura, T. Spectroscopic characterization of heterogeneous structure of *Samia cynthia ricini* silk fibroin induced by stretching and molecular dynamics simulation. *Macromolecules* **37**, 3497–3504 (2004).

[17] Rousseau, M. E., Lefevre, T., Beaulieu, L., Asakura, T. & Pezolet, M. Study of protein conformation and orientation in silkworm and spider silk fibres using Raman microspectroscopy. *Biomacromolecules* **5**, 2247–2257 (2004).

[18] Rousseau, M. E., Beaulieu, L., Lefèvre, T., Paradis, J., Asakura, T. & Pèzolet, M. Characterization by Raman microspectroscopy of the strain-induced conformational transition in fibroin fibres from the silkworm *Samia cynthia ricini*. *Biomacromolecules* **7**, 2512–2521 (2006).

[19] Lefèvre, T., Rousseau, M. E. & Pézolet, M. Protein secondary structure and orientation in silk as revealed by Raman spectromicroscopy. *Biophys. J.* **92**, 2885–2895 (2007).

[20] Boulet-Audet, M., Vollrath, F. & Holland, C. Identification and classification of silks using infrared spectroscopy. *J. Exp. Biol.* **218**, 3138–3149 (2015).

[21] Guo, C., Zhang, J., Jordan, J. S., Wang, X., Henning, R. W. & Yarger, J. L. Structural comparison of various silkworm silks: An insight into the structure–property relationship. *Biomacromolecules* **19**, 906–917 (2018).

[22] van Beek, J. D., Beaulieu, L., Schäfer, H., Demura, M., Asakura, T. & Meier, B. H. Solid-state NMR determination of the secondary structure of *Samia cynthia ricini* silk. *Nature* **405**, 1077–1079 (2000).

[23] Nakazawa, Y. & Asakura, T. Structure determination of a peptide model of the repeated helical domain in *Samia cynthia ricini* silk fibroin before spinning by a combination of advanced solid-state NMR methods. *J. Am. Chem. Soc.* **125**, 7230–7237 (2003).

[24] Asakura, T., Nishimura, A., Kametani, S., Kawanishi, S., Aoki, A., Suzuki, F., Kaji, H. & Naito, A. Refined crystal structure of *Samia cynthia ricini* silk fibroin revealed by solid-state NMR investigations. *Biomacromolecules* **18**, 1965–1974 (2017).

[25] Takahashi, Y., Gehoh, M. & Yuzuriha, K. Crystal structure of silk (*Bombyx mori*). *J. Polym. Sci. Polym. Phys.* **29**, 889–891 (1991).

[26] Asakura, T., Kuzuhara, A., Tabeta, R. & Saito, H. Conformation characterization of *Bombyx mori* silk fibroin in the solid state by high-frequency $^{13}C$ cross polarization-magic angle spinning NMR, X-ray diffraction, and infrared spectroscopy. *Macromolecules* **18**, 1841–1845 (1985).

[27] Suzuki, Y., Kawanishi, S., Yamazaki, T., Aoki, A., Saito, H. & Asakura, T. Structural determination of the tandem repeat motif in *Samia cynthia ricini* liquid silk by solution NMR. *Macromolecules* **48**, 6574–6579 (2015).

[28] Fang, G., Sapru, S., Behera, S., Yao, J., Shao, Z., Kundu, S. C. & Chen, X. Exploration of the tight structural–mechanical relationship in mulberry and non-mulberry silkworm silks. *J. Mater. Chem. B* **4**, 4337–4347 (2016).

[29] Malay, A. D., Sato, R., Yazawa, K., Watanabe, H., Ifuku, N., Masunaga, H., Hikima, T., Guan, J., Mandal, B. B., Damrongsakkul, S. & Numata K. Relationships between physical properties and sequence in silkworm silks. *Sci. Rep.* **6**, 27573 (2016).

[30] Chen, F., Porter, D. & Vollrath, F. Structure and physical properties of silkworm cocoons. *J. R. Soc. Interface* **9**, 2299–2308 (2012).

[31] Takahashi, Y., Sumita, I. & Tadokoro, H. Structural studies of polyethers. IX. Planar zigzag modification of poly(ethylene oxide). *J. Polym. Sci. Pol. Phys.* **11**, 2113–2122 (1973).

[32] Hearle, J. W. S. A critical review of the structural mechanics of wool and hair fibres. *Int. J. Biol. Macromol.* **27**, 123–138 (2000).

[33] Paquin, R. & Colomban, P. Nanomechanics of single keratin fibres : A Raman study of the $\alpha$-helix → $\beta$-sheet transition and the effect of water. *J. Raman Spectrosc.* **38**, 504–514 (2007).

[34] Toki, S., Fujimaki, T. & Okuyama, M. Strain-induced crystallization of natural rubber as detected real-time by wide-angle X-ray diffraction technique. *Polymer* **41**, 5423–5429 (2000).

[35] Kondo, Y., Hirabayashi, K., Iizuka, E. & Go, Y. Studies of the fine structure of silk fibroin: (III). Confirmation of the prescence of helical conformation in *Anteraea pernyi* silk fibroin. *Sen-I Gakkaishi* **23**, 311–315 (1967).

[36] Hirabayashi, K., Ishikawa, H. & Kakudo, M. Changes in the internal fine structure of silk fibroin by drawing. *Sen-I Gakkaishi* **25**, 440–446 (1968).

[37] Nakazawa, Y., Bamba, M., Nishio, S. & Asakura, T. Tightly winding structure of sequential model peptide for repeated helical region in *Samia cynthia ricini* silk fibroin studied with solid-state NMR. *Protein Sci.* **12**, 666–671 (2003).

[38] Asakura, T., Ito, T., Okudaira, M. & Kameda, T. Structure of alanine and glycine residues of *Samia c ynthia ricini* silk fibres studied with solid-state $^{15}N$ and $^{13}C$ NMR. *Macromolecules* **32**, 4940–4946 (1999).

[39] Magoshi, J., Magoshi, Y. & Nakamura, S. Mechanism of fibre formation of silkworm. In *Silk polymers*, ACS Symposium Series; American Chemical Society: Washington, D.C, WA, USA. Vol. 544, Chapter 25, 292–310 (1993).

[40] Freddi, G., Monti, P., Nagura, M., Gotoh, Y. & Tsukada, M. Structure and molecular conformation of Tussah silk fibroin films: Effect of heat treatment. *J. Polym. Sci. Polym. Phys.* **35**, 841–847 (1997).

[41] Yoshioka, T. & Kameda, T. X-ray scattering analyses quantitatively revealed periodic hierarchical structure of polyalanine $\beta$-sheet and non-polyalanine amorphous domains in *Antheraea assamensis* (Muga) silk. *J. Silk Sci. Tech. Jpn* **27**, 95–101 (2019).

[42] Yoshioka, T., Tashiro, K. & Ohta, N. Molecular orientation enhancement of silk by the hot-stretching-induced transition from $\alpha$-helix-HFIP complex to $\beta$-sheet. *Biomacromolecules* **17**, 1437–1448 (2016).

[43] Drummy, L. F., Farmera, B. L., & Naik, R. R. Correlation of the $\beta$-sheet crystal size in silk fibers with the protein amino acid sequence. *Soft Matter* **3**, 877–882 (2007).

[44] Balcytis, A., Ryu, M., Wang, X., Novelli, F., Seniutinas, G., Du, S., Wang, X., Li, J., Davis, J., Appadoo, D., Morikawa, J. & Joudkazis, S. Silk: Optical properties over 12.6 octaves THz-IR-Visible-UV range. *Materials* **10**, 356 (2017).

[45] Bamford, C. H., Brown, L., Elliot, A., Hanby, W. E. & Trotter, I. F. Alpha and beta-forms of poly-L-alanine. *Nature* **173**, 27–29 (1954).

[46] Brown, L. & Trotter, I. F. X-ray studies of poly-L-alanine. *Trans. Faraday Soc.* **52**, 537–548 (1956).

[47] Li, M., Wu, Z., Zhang, C., Lu, S., Yan, H., Huang, D. & Ye, H. Study on porous silk fibroin materials. II. Preparation and characteristics of spongy porous silk fibroin materials. *J. Appl. Polym. Sci.* **79**, 2192–2199 (2001).

[48] Nazarov, R., Jin, H. & Kaplan, D. L. Porous 3-D scaffolds from regenerated silk fibroin. *Biomacromolecules* **5**, 718–726 (2004).

[49] Vollrath, F. & Knight, D. P. Liquid crystalline spinning of spider silk. *Nature* **410**, 541–548 (2001).

[50] Tucker, C. L., Jones, J. A., Bringhurst, H. N., Copeland, C. G., Addison, J. B., Weber, W. S., Mou, Q., Yarger, J. L. & Lewis, R. V. Mechanical and physical properties of recombinant spider silk films using organic and aqueous solvents. *Biomacromolecules* **15**, 3158–3170 (2014).

[51] Rajkhowa, R., Kaur, J., Wang, X. & Batchelor, W. Intrinsic tensile properties of cocoon silk fibres can be estimated by removing flaws through repeated tensile tests. *Interface* **12**, 20150177 (2015).

[52] Offord, C., Vollrath, F. & Holland, C. Environmental effects on the construction and physical properties of *Bombyx mori* cocoons. *J. Mater. Sci*. **51**, 10863–10872 (2016).

[53] Hu, X., Shmlev, K., Sun, L., Gil, E. S., Park, S. H., Cebe, P. & Kaplan, D. L. Regulation of silk material structure by temperature-controlled water vapor annealing. *Biomacromolecules* **12**, 1686–1696 (2011).

[54] Guan, J., Porter, D. & Vollrath, F. Thermally induced changes in dynamic mechanical properties of native silks. *Biomacromolecules* **144**, 930–937 (2013).

## Chapter III

## Structure Water-Solubility Relationship in *α*-Helix-Rich Films Cast from Aqueous and 1,1,1,3,3,3-Hexafluoro-2-Propanol Solutions of *S. c. ricini* Silk Fibroin

### 3.1. Introduction

Fibre spun by the domesticated wild silkworm, *S. c. ricini*, is essentially different from that spun by the mulberry silkworm, *B. mori*. While the primary structure of *S. c. ricini* silk fibroin contains repeat poly-L-alanine sequences [$(Ala)_{12–13}$] [1] that predominantly form a water-soluble *α*-helix structure [2], that of *B. mori* contains a $(GAGAGS)_n$ repeat motif [3] that forms the metastable silk I structure [4]. During natural spinning by mature *S. c. ricini* larvae, *α*-helix to *β*-sheet transition occurs and the native silk produced is insoluble in water [2,5,6]. Materials (in various morphologies) such as films, gels, nanoparticles, and sponges can be fabricated from *S. c. ricini* silk fibroin solutions in water or organic solvents such as 1,1,1,3,3,3-hexafluoro-2-propanol (HFIP) and trifluoroacetic acid (TFA). Due to the difference in primary structure, such biomaterials may exhibit different material and biomedical properties that may be handy in the design and development of novel biomaterials. Therefore, regeneration of *S. c. ricini* cocoon silk fibroin is required to obtain solutions for fabrication. However, owing to the unique structure of *S. c. ricini* silk fibroin, attempts to use the traditional regeneration protocols for *B. mori* have been unsuccessful. For instance, silk fibroin powder [7] and fibre [8] regenerated from *S. c. ricini* cocoons had lower molecular weight and diminished fibre tenacity, respectively, due to hydrolysis resulting from relatively harsh preparative conditions such as degumming temperature. This has limited effective utilization of this unique bioresource [9].

To overcome this shortcoming, fabrication of biomaterials using liquid fibroin obtained directly from the posterior silk glands of mature *S. c. ricini* larvae has been explored [5,10,11]. As already clarified in the preceding chapter, films cast from *S. c. ricini* aqueous liquid fibroin

($LF_{aq}$ as-cast film) at room temperature (~23 °C) (processing route indicated by red arrows in chapter I) were *α*-helix-rich. In addition, it takes several minutes to collect workable amounts of liquid fibroin from the posterior silk glands of *S. c. ricini*, that is, this fabrication approach is a time-consuming downside, if large-scale applications are desirable. Moreover, the $LF_{aq}$ as-cast films are water-soluble [5,10], and require post-treatment to render them water stable, a desirable property for wet-state applications. *β*-sheet formation, often induced by treatment with aqueous alcohol solutions, and thermal- and water-vapor annealing is the most widely used strategy to render the biomaterials water stable [12-16]. However, such post-treatments often modify inherent desirable properties of the fibroin materials, limiting their applicability [9,12]. Thus, the need for an alternative fabrication strategy for *S. c. ricini* silk, and indeed other wild silks, is imperative, owing to their attractive mechanical properties, biocompatibility, biodegradation, abundant yields in nature, and promising applications [9,17].

Recently, Yoshioka et al developed a mild approach for fabricating high-molecular-weight, water-resistant as-cast films directly, that is, without the need of the time-consuming steps as well as post-product treatment, from *B. mori* silk gland fibroin (SGF) [12]. However, the cast film obtained was *β*-sheet-rich and very long dissolution durations (>60 days) were required to afford *α*-helix-rich as-cast films. If this fabrication approach is successfully applied to *S. c. ricini* silk gland fibroin, one can expect to obtain *α*-helix-rich cast film because of the fibroin proteins' characteristic poly-L-alanine repeat sequences. In addition to the conventional *β*-sheet-rich films, such a film is highly desirable and will widen the scope of potential applications of silk fibroin-based films [18].

In this chapter, the author successfully applied a similar strategy in the fabrication of *S. c. ricini* silk gland cast films as summarized in figure 1-1 in chapter I (processing route indicated by blue arrows). As earlier reported for *B. mori* silk fibroin [12], preliminary studies and the current study also revealed 40% ethanol/water solution (v/v; 40%-EtOH) to be the

optimum concentration that gave a gel of *S. c. ricini* silk gland fibroin that was easy to separate from the rest of the silk gland, and soluble in HFIP. The solution of the gel (herein, SGF-gel) in HFIP was transparent. Films were cast from this solution at room temperature (herein, $SGF_{HFIP}$ as-cast film) and compared to the conventional ones cast from an aqueous solution liquid fibroin ($LF_{aq}$) prepared as escribed in the preceding chapter.

The structure and properties of the cast films were systematically investigated in detail by thermal analyses, $^{13}C$ solid-state NMR spectroscopy, Fourier transform infra-red spectroscopy (FTIR), wide-angle X-ray diffraction (WAXD), high performance liquid chromatography (HPLC), and gel permeation chromatography (GPC). Our results revealed a structure water-solubility relationship in the $LF_{aq}$ and $SGF_{HFIP}$ *S. c. ricini* as-cast films. Based on these experimental results, a plausible model of the mechanism leading to water resistance of the $SGF_{HFIP}$ as-cast film is proposed.

### 3.2. Materials and Methods

#### 3.2.1. Fabrication of Cast Films

*S. c. ricini* silkworm larvae were reared in the laboratory on an all-instar artificial diet, SilkMate L4M (Nosan Corp., Yokohama, Japan) under the conditions already outlined in chapter II. Late fifth instar larvae were sub-divided into three batches. The larvae in the first batch were dissected to obtain intact silk glands. The glands were carefully rinsed in Milli-Q water and kept refrigerated immersed in different concentrations of aqueous ethanol (% v/v) (Wako Pure Chemical Industries Ltd, Osaka, Japan) to induce gelation of fibroin [12] in the lumen of the posterior division of the silk glands. Gelation of the silk fibroin in silk glands immersed in aqueous with concentrations greater than 30 % was visually observed to occur after about 3 h under these conditions. The silk gland is longitudinally differentiated into functionally distinct posterior (PSG), middle (MSG), and anterior (ASG) sections [19]. The PSG, where fibroin is synthesized and stored as a weak gel before spinning, was separated from

the middle and anterior sections and its epithelium was carefully peeled to obtain the solidified silk gland fibroin gel (SGF-gel). The SGF-gel obtained was dissolved in neat HFIP (99.0%; Tokyo Chemical Industry Company Limited, Tokyo, Japan) in sealed screw cap tubes under mild agitation at 23 ± 2 °C. However, the posterior silk gland of *S. c. ricini* are thin and flexuous and long durations would be required to obtain workable amounts of SGF-gel. We hypothesized that only the SGF-gel would dissolve in HFIP if whole (unpeeled) 40%-EtOH-treated PSG were dissolved. To test this hypothesis, about 2.0 cm portions of the unpeeled PSG were dissolved in HFIP under mild agitation at room temperature. The SGF-gel in the gland lumen dissolved within several hours (~2 h) and the undissolved epithelium was separated from the fibroin solution by sedimentation or filtration. For comparison, aqueous liquid fibroin from the posterior silk glands of the second batch of larvae was collected as descried in chapter II.

Films were prepared by separately casting the silk fibroin solutions onto polystyrene Petri-dishes. After drying at 23 ± 2 °C and a relative humidity of 30 ± 2%, transparent and flexible films that could be peeled off the substrate were obtained. The thickness of the cast films was controlled by adjusting the concentration or volume of the fibroin solutions cast.

The third batch of the larvae were let to spin cocoons. These were cut open by a pair of scissors to remove the pupae and for all analyses, portions of the native fibre were sampled from the middle section of the middle layer of the fresh cocoons.

The as-cast films and native fibre were heat-, HFIP-gas-, water- and EtOH-treated and used for the respective analyses as described in sub-sections 3.2.4 through 3.2.8. For heat-treatment, rectangular portions of the $LF_{aq}$ and $SGF_{HFIP}$ as-cast films, and native fibre were were sandwitched (separately) between thin glass slides (~1.0 mm thick) alongside a sensitive thermocouple to directly monitor the temperature of the sample. These were then heated on a digital hot-plate (Corning PC-420D) to 220 °C, and kept at this temperature (annealed) for 1 min. For HFIP-gas-treatment, the $LF_{aq}$ as-cast film was placed in a container saturated with

HFIP gas at 23, 30, 40 and 50 °C for 0.3, 3/2, 1, 2, 3, 4, 5, and 6 h to obtain various HFIP-gas-treated films. For water-treatment, portions of the $SGF_{HFIP}$ as-cast films were immersed in water for 12 h and dried at room temperature. Lastly, for EtOH-treatment, the $LF_{aq}$ and $SGF_{HFIP}$ as-cast films were immersed in aqueous 80%-EtOH for 12 h, dried at room temperature.

### 3.2.2. Determination of Molecular Weight (Mw)

Molecular weight distributions of the SGF-gel and $LF_{aq}$ as-cast film were determined by gel permeation chromatography (GPC). For each measurement, about 20 mg of the fibroin protein sample was dissolved in hexafluoroacetone trihydrate at 23 ± 2 °C for 24 h. The concentration of the solution was adjusted to about 0.02 wt% with the eluent (HFIP) containing 1.0 mL of 5.0 mM sodium trifluoroacetate and filtered using a 5.0 $\mu$m polytetrafluoroethylene (PTFE) filter syringe. The chromatographic set-up comprised of a HLC-8320GPC system (Tosoh Corp., Tokyo, Japan) fitted with a 4.6 mm i.d. × 3.5 cm, 4 $\mu$m TSKgel SuperH-H guard column (Tosoh Corp., Tokyo, Japan), two (6.0 mm i.d. × 15 cm, 3.0 and 5.0 $\mu$m, TSKgel SuperHM-H separation columns (Tosoh Corp., Tokyo, Japan), and a dual flow refractive index (RI) detector (Tosoh Corp., Tokyo, Japan). The standard $M_W$ markers were polymethyl methacrylate (PMMA) in the range 0.55 to 2,100 kDa.

### 3.2.3. Amino Acid Composition Analysis

The amino acid compositions of the films cast from liquid fibroin and SGF-HFIP solutions obtained by dissolution of the SGF-gel (with and without peeling) of the gland epithelium were evaluated by high performance liquid chromatography (HPLC). For each measurement, about 5.0 mg of the fibroin protein was hydrolysed in 6 M HCl at 110 ℃ for 22 h and dried with a $N_2$ purge. The hydrolysates were dissolved in 500 $\mu$L of citric acid buffer (pH 2.2), and de-proteinized by centrifugal filtration (Ultrafree-MC 0.45 $\mu$m, 13,400 rpm, 2 min). An analytical blank was similarly prepared. Each filtrate was appropriately diluted and

analysed by a post-column derivatization with *o*-phthalaldehyde (OPA) and N-acetyl-L-cysteine using a HPLC system (Shimadzu, LC-VP) equipped with a Shim-pack Amino-Na (100 mm L × 6.0 mm i.d.) cation exchange column (Shimadzu, Japan) and an ISC-30/S0504 Na (50 mm L × 4.0 mm i.d.) ammonia trap column. A gradient elution was performed in the high-pressure mode using sodium citrate buffers (A) and (B) and sodium hydroxide (C) as mobile phases at a flow rate of 0.4 mL $min^{-1}$. The column temperature and injection volume were 60 °C and 10$\mu$L, respectively. A Shimadzu RF-20A$_{XS}$ fluorescence detector was used to detect the fluorescence products at excitation and emission wavelengths of 350 and 435 nm, respectively. 10-fold dilutions of the amino acid mixture standard solution type H (Wako Pure Chemical Industries Ltd., Osaka, Japan) were analysed to obtain a calibration curve used for quantitation of each component.

### 3.2.4. Fourier Transform Infra-red (FTIR) Spectroscopy

FTIR measurements of the as-cast, and heat-, HFIP-gas-, water- and EtOH-treated $LF_{aq}$ and $SGF_{HFIP}$ films were recorded at room temperature with an FTIR-620 (JASCO International Co. Ltd., Japan) spectrometer in the transmission mode as described in chapter II. For each measurement, 32 scans were co-added in the spectral range 4000 to 400 $cm^{-1}$ with a 2 $cm^{-1}$ resolution. The resultant spectrum was corrected by subtracting a background spectrum recorded under similar scan conditions. The assignments of conformation sensitive bands for *S. c. ricini* silk fibroin and HFIP used in this report were: ~1625 and ~1519 $cm^{-1}$ as $\beta$-sheet structure [20,21], ~1658 and 1545 - 1548 $cm^{-1}$ as $\alpha$-helix [11,20], and ~894, ~736 and ~686 $cm^{-1}$ as characteristic peaks assigned to HFIP [22].

### 3.2.5. $^{13}$C Cross Polarization – Magic Angle Spinning Solid-State NMR Spectroscopy

$^{13}$C CP/MAS solid-state NMR measurements of native fibre, and the $LF_{aq}$ and $SGF_{HFIP}$ as-cast films were carried out with a Bruker Avance 600 WB (Karlsruhe, Germany)

spectrometer with a magnetic field of 14.1 T at room temperature as described in chapter II. The spectrometers were operated at a $^{13}C$ NMR frequency of 150.94 MHz. For each measurement, the fibroin protein sample was cut into small pieces, packed into a solid-state probe and spun at a MAS frequency of 10.0 kHz in a 4.0 mm Ø zirconia rotor sample tube. A $^{1}H$ 90° pulse length of 3.5 $\mu$s and $^{1}H$-$^{13}C$ cross-polarization (CP) contact of 70 kHz were employed for the CP experiments. High-power $^{1}H$ decoupling using the SPINAL-64 method was employed. The CP experiments were repeated every 3.0 s and the $^{13}C$ chemical shifts were calibrated externally through the adamantane methylene peak at 29.5 ppm relative to TMS at 0 ppm.

### 3.2.6. Thermal Analyses

Differential scanning calorimetry (DSC) measurements of native fibre and heat-, HFIP-gas-, water- and EtOH-treated $LF_{aq}$ and $SGF_{HFIP}$ films were performed with a DSC Q200 analysis system (TA Instruments, USA). Instrument calibration for heat flow and temperature were done using indium, whereas for heat capacity, aluminum and sapphire were used. For each measurement, about 5.0 mg of the fibroin protein sample was encapsulated in an aluminum pan and heated between -30 and 430 °C at 2 °C $min^{-1}$ under a dry nitrogen nitrogen gas flow of 50 mL $min^{-1}$. The weight loss profiles of the the silk fibroin solutions, native fibre and heat-, HFIP-gas-, water- and EtOH-treated $LF_{aq}$ and $SGF_{HFIP}$ films were determined by thermal gravimetry (TG) with a Thermoplus TG 8120 system (Rigaku Corp., Tokyo, Japan). For each measurement, about 1.0 mg of the fibroin protein sample was heated in an aluminium pan from room temperature to 430 °C at a heating rate of 2 °C $min^{-1}$ under a dry nitrogen gas flow of 200 mL $min^{-1}$.

### 3.2.7. Wide-Angle X-ray Diffraction Analyses

WAXD measurements of native fibre and heat-, HFIP-gas-, water- and EtOH-treated $LF_{aq}$ and $SGF_{HFIP}$ films were carried out with a 3.5 m NANOPIX X-ray diffractometer (Rigaku Corp., Tokyo, Japan) (40 kV, 30 mA, CuKα 1.5418 Å radiation) equipped with a highly sensitive single-photon counting pixel HyPix-6000 2D detector with a pixel size of 100 × 100 $\mu m^2$ (Rigaku Corp., Tokyo, Japan) as previously described [23]. Calibration of the camera distance, subtraction of background diffraction and air-scattering, extraction of 2$\theta$-profiles from the 2-dimensional WAXD patterns, estimation of the the crystallite size, and correction for instrumental peak broadening effect were carried out as detailed in sub-section 2.2.4. in the preceding chapter.

### 3.2.8. Wet-Drawing of the Cast Films

Wet-drawability of as-cast $SGF_{HFIP}$, and 80%-EtOH-treated $SGF_{HFIP}$ and $LF_{aq}$ films were evaluated by manually drawing rectangular strips (2 × 10 mm) of the films using a hand-held stretching device while immersed in water (wet-drawing) at room temperature until break (maximum draw ratio, $\varepsilon$). The diameter of the strips was ~20 $\mu$m and 19 replicate samples for each test film were drawn.

## 3.3. Results and Discussion

### 3.3.1. Structure and Properties of the $LF_{aq}$ and $SGF_{HFIP}$ As-Cast Films

Immersion of freshly extracted *S. c. ricini* silk glands in 40%-EtOH induced $\beta$-sheet formation in the fibroin in the lumen of the posterior silk glands within a few hours (~3 h; visual observation) and peeling the gland epithelium gave a transparent silk gland fibroin gel (SGF-gel). WAXD 2$\theta$-profiles of the wet SGF-gel in the wet (in 40%-EtOH) and dry-states were as shown in Figure 3-1. Compared to the $\beta$-sheet-rich profile of *S. c. ricini* native fibre (see profile IV), the SGF-gel already exhibited a $\beta$-sheet profile in the wet-state (profile I). However, this profile was somehow distorted, probably due to a high amount of adsorbed EtOH

and bulk water. When the SGF-gel was dried, at room temperature or by freeze-drying, most of the EtOH and bulk water were removed or substantially reduced and the profiles of the two dry-states (see profiles II and III) became evidently $\beta$-sheet-rich.

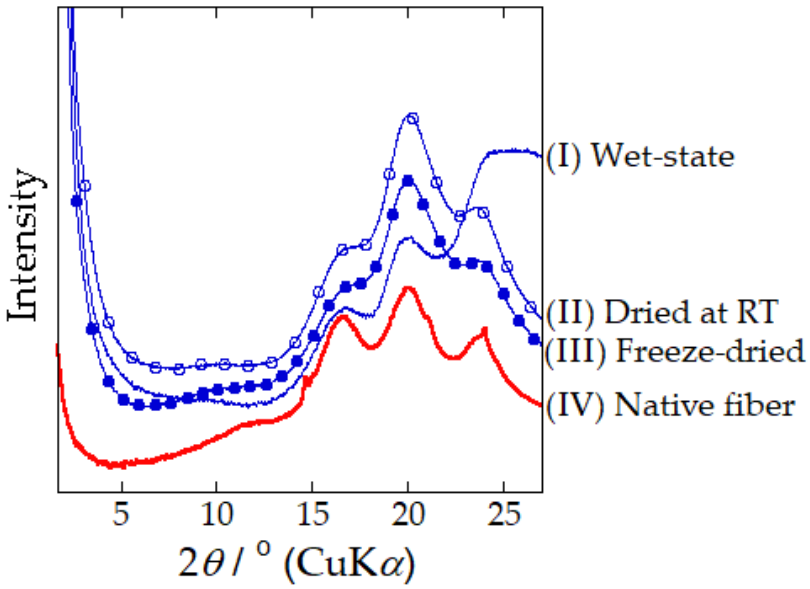


**Figure 3-1**

**WAXD 2$\theta$-profiles of *S. c. ricini* silk gland fibroin gel (SGF-gel) in the wet- and dry-states. Profile I is for the wet-state gel (in 40%-EtOH), II is for the gel dried at room temperature, III is for the freeze-dried gel, and IV is for native fibre.**

To evaluate the purity of the SGF-gel, its molecular weight distribution was evaluated by gel permeation chromatography (GPC) and compared to that of a conventional film cast from aqueous liquid fibroin ($LF_{aq}$ as-cast film) prepared by dissolution of silk dope obtained directly from the silk glands of mature *S. c. ricini* larvae in water. The differential molecular weight distribution of the SGF-gel was essentially similar to that of the $LF_{aq}$ as-cast film as shown in Figure 3-2. This demonstrates good separation of the SGF-gel from the rest of the silk gland (epithelium and sericin layers) in the current fabrication strategy.

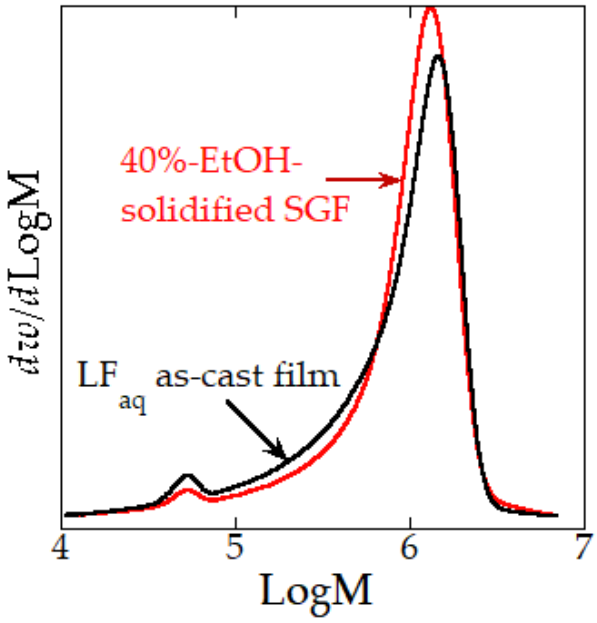


**Figure 3-2**

**Differential molecular weight distributions of the SGF-gel (curve in red) and $LF_{aq}$ as-cast film (curve in black).**

HFIP is known to be an excellent solvent for various kinds of peptides and proteins [24-26] including *B. mori* silk fibroin in an amorphous state [27-29] and spider silk [30]. It causes negligible molecular weight damage [27,31], and induces and stabilizes the $\alpha$-helical conformation [22,32]. On the other hand, once silk fibroin forms the $\beta$-sheet crystal, it hardly dissolves, even in HFIP [30]. However, the SGF-gel which forms an imperfect $\beta$-sheet structure when treated with 40%-EtOH [12], dissolved in HFIP within 2 h at 23 ± 2 °C under mild agitation to give a transparent solution. FTIR results of films cast from solutions prepared by dissolution of the SGF-gel in HFIP ($SGF_{HFIP}$ as-cast films) at 23 ± 2 °C for different durations (between 1.25 and 24 h) were as shown in Figure 3-3. These results suggest that the dissolution of the SGF-gel in HFIP does not depend on the dissolution duration.

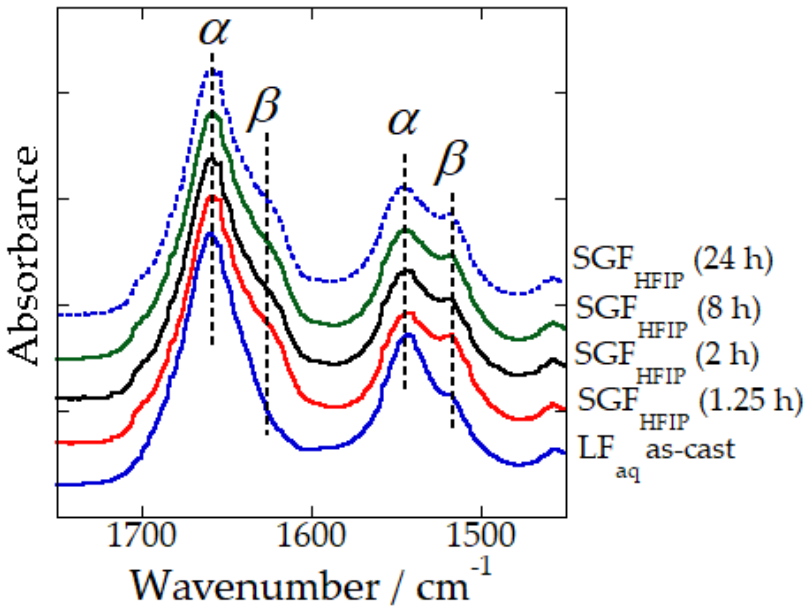


**Figure 3-3**

**FTIR spectra of $SGF_{HFIP}$ films cast from solutions prepared by dissolution of *S. c. ricini* SGF-gel in HFIP at 23 ± 2 °C for 1.25, 2, 8, and 24 h.**

Further, the amino acid composition analyses of the film cast from a solution of the SGF-gel in HFIP for 2 h, $SGF_{HFIP}$ (a), and the $LF_{aq}$ as-cast film were as shown in Table 2-1. The molar ratios of Ser residues in the $SGF_{HFIP}$ (a) and $LF_{aq}$ as-cast films were comparable. As already mentioned in the Mw distribution, these results further demonstrate the successful separation of *S. c. ricini* SGF from the silk glands in a form that is easy to dissolve in HFIP.

**Table 2-1.** Amino acid compositions (mol %) of films cast from aqueous liquid fibroin ($LF_{aq}$) and 1,1,1,3,3,3-hexafluoro-2-propanol (HFIP) solutions of the 40%-EtOH-treated posterior silk gland (PSG) $SGF_{HFIP}$ with (**a**) and without (**b**) peeling the gland epithelium.

| **Amino acid** | **$LF_{aq}$** | **$SGF_{HFIP}$ (a)** | **$SGF_{HFIP}$ (b)** |
|---|---|---|---|
| Gly | 33.8 | 34.5 | 34.9 |
| Ala | 44.2 | 40.0 | 41.3 |
| Pro | 0.4 | 0.5 | 0.5 |
| Val | 0.5 | 0.5 | 0.6 |
| Leu | 0.4 | 0.5 | 0.5 |
| Ile | 0.4 | 0.4 | 0.4 |
| Met* | * | * | * |
| Ser | 6.1 | 7.2 | 5.6 |
| Thr | 0.5 | 0.8 | 0.7 |
| Cys* | * | * | * |
| Asx** | 3.7 | 4.0 | 4.0 |
| Glx** | 0.9 | 1.0 | 1.1 |
| Arg | 1.8 | 2.1 | 2.1 |
| Lys | 0.4 | 0.5 | 0.5 |
| His | 1.6 | 1.8 | 1.9 |
| Tyr | 5.3 | 6.3 | 5.9 |
| Phe | 0.3 | 0.2 | 0.2 |
| Trp# | - | - | - |
| **Gly/Ala** | **0.8** | **0.9** | **0.9** |
| **Acidic** | **4.6** | **5.0** | **5.1** |
| **Basic** | **3.8** | **4.3** | **4.5** |

*Met and Cys were below the quantitation limit of the current analytical method. Further, under conventional acid hydrolysis, #Trp is generally not recovered and $^{\$}$Asn and $^{\$}$Gln are de-aminated to Asp and Glu, respectively.

Similar to the *S. c. ricini* $LF_{aq}$ as-cast film already reported in chapter II, the $SGF_{HFIP}$ as-cast film was transparent and flexible as shown in Figure 3-4.


**Figure 3-4**

**A transparent and flexible $SGF_{HFIP}$ film cast from a solution obtained by dissolution of the SGF-gel in HFIP at 23 ± 2 °C for 12 h.**

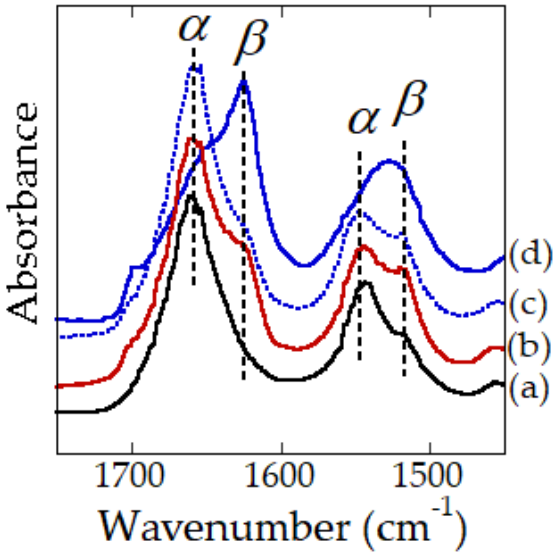


**Figure 3-5**

**FTIR spectra of films cast from silk fibroin solutions obtained by dissolution of 40%-EtOH-solidified *B. mori* SGF for 10 days (spectrum d) and 90 days (spectrum c), and *S. c. ricini* SGF for 12 h in HFIP (spectrum b) at 23 ± 2 °C. Spectrum (a) is that of the film cast from an aqueous solution of *S. c. ricini* liquid fibroin.**

FTIR results of the $LF_{aq}$ and $SGF_{HFIP}$ as-cast films were as shown in Figure 3-5a,b. Both films were $\alpha$-helix-rich as seen in the amide I and II bands of their spectra. These results were well supported by $^{13}C$ solid-state NMR results shown in Figure 3-6. Unlike the case of *B. mori* SGF-gel in our recent report in which long dissolution durations (>60d) were necessary to obtain $\alpha$-helix-rich as-cast films (Figure 3-5c,d) [12], a short-dissolution duration was sufficient for *S. c. ricini* SGF-gel. This was speculated to result from the rich content of Ala residues (~45 mol%) in the silk fibroin [1], an intrinsically $\alpha$-helix-stabilizing amino acid [33]. Moreover, the stability of the $\alpha$-helical conformation has also been ascribed to a winding phenomenon typical to the N- and C-termini of the poly-L-alanine sequences of *S. c. ricini* silk fibroin [34].

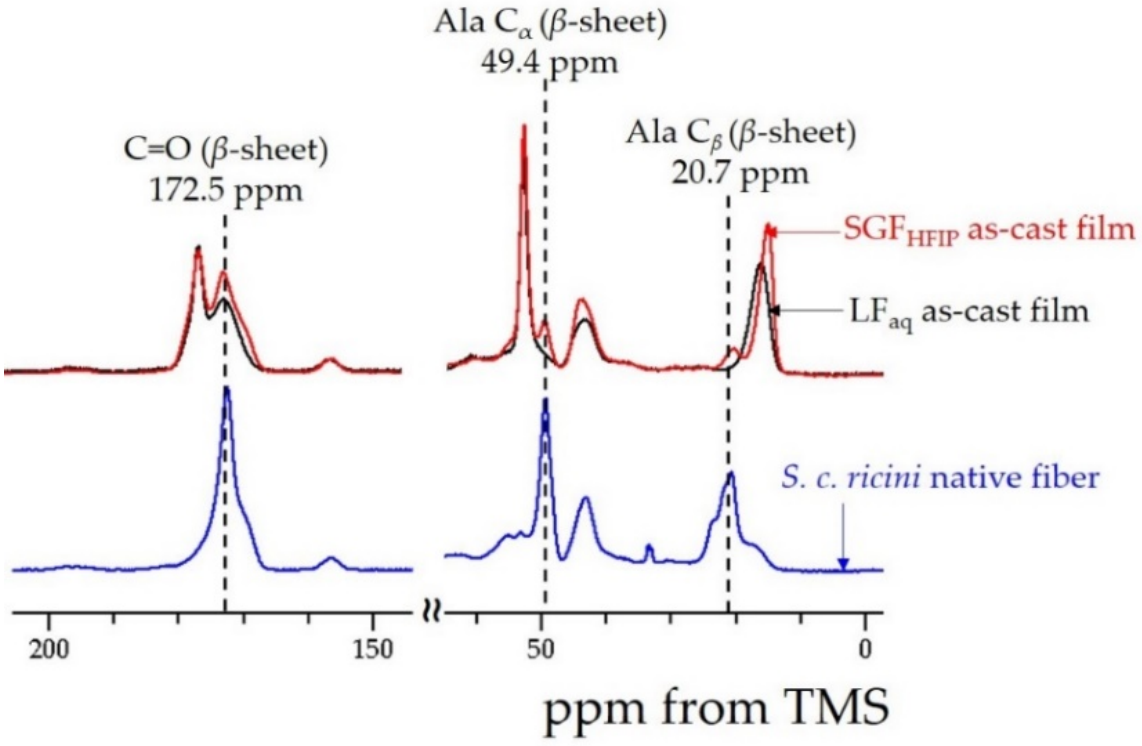


**Figure 3-6**

**$^{13}C$ solid-state NMR spectra in the ranges 0 to 55 and 150 to 200 ppm of *S. c. ricini* native fibre (spectrum in blue), and $LF_{aq}$ (spectrum in black) and $SGF_{HFIP}$ (spectrum in red) as-cast films.**

The $LF_{aq}$ as-cast film dissolved almost immediately when placed on a water surface, whereas the $SGF_{HFIP}$ as-cast one remained afloat for more than two weeks (see Figure 3-5). The molecular weight of silk fibroin has been reported to influence its solubility in water [35]. However, the differential molecular weight distributions of the SGF-gel and $LF_{aq}$ as-cast film were essentially similar as already mentioned (Figure 3-2). This implies that the molecular weight of the silk firoin samples did not possibly contribute to the difference observed in water resistance.

In Chapter II, the amide I region of the FTIR spectrum of the $LF_{aq}$ as-cast film was assigned to the $\alpha$-helical conformation, whereas the amide II region was speculated to contain some amount of $\beta$-sheet or other components. In this study, detailed comparative examination of the FTIR spectra of the $LF_{aq}$ and $SGF_{HFIP}$ as-cast films confirmed a small but highly reproducible: The $SGF_{HFIP}$ as-cast film clearly had some $\beta$-sheet content in the amide I and II regions. This difference was also discernible in the NMR results as shown in the chemical shifts highlighted in Figure 3-6.

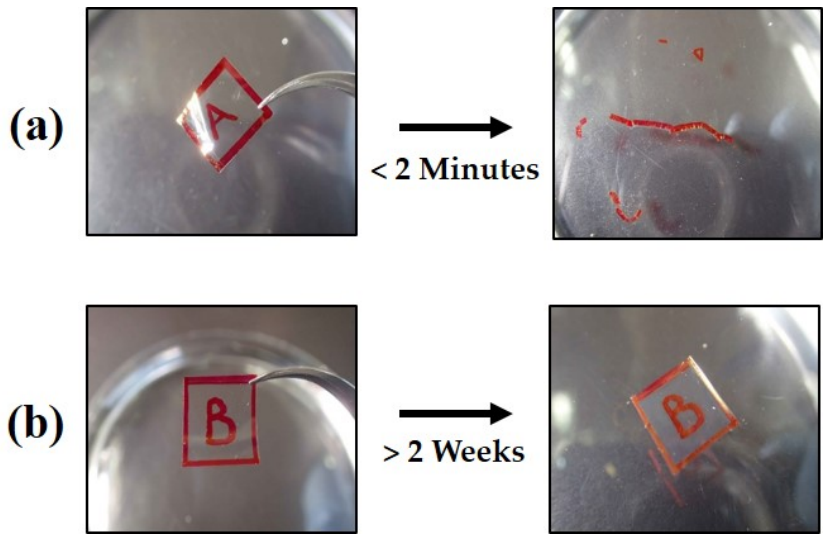


**Figure 3-7**

**Water solubility of *S. c. ricini* $LF_{aq}$ (a) and $SGF_{HFIP}$ (b) as-cast films.**

### 3.3.2. Ordered $\alpha$-Helix Structure in the $SGF_{HFIP}$ As-Cast Film

WAXD $2\theta$-profiles of the $LF_{aq}$ and $SGF_{HFIP}$ as-cast films compared to that of a $\beta$-sheet-rich dry SGF-gel are shown in Figure 3-8. Weak, but distinct and reproducible wide-angle scattering peaks (obtained by MoKα 0.7083 Å radiation) assigned to the $\beta$-sheet conformation were observed at $2\theta = 18.2°$ (2.3 Å: corresponding to the $\beta_{210}$ reflection) and $2\theta = 19.7°$ (2.1 Å: corresponding to the $\beta_{103}$ reflection) in the profile for the $SGF_{HFIP}$ as-cast film, but absent in that of the $LF_{aq}$ as-cast film. This confirmed the FTIR and NMR results regarding the presence of some $\beta$-sheet structure in the $SGF_{HFIP}$ as-cast film. On the other hand, a sharp and intense peak at $2\theta = 5.5°$ (corresponding to 7.4 Å) was observed for the $LF_{aq}$ as-cast film but absent in the dry SGF-gel. This peak implied the existence of long-range order and was clarified to correspond to ordered aggregation of the $\alpha$-helix structure in Chapter II.

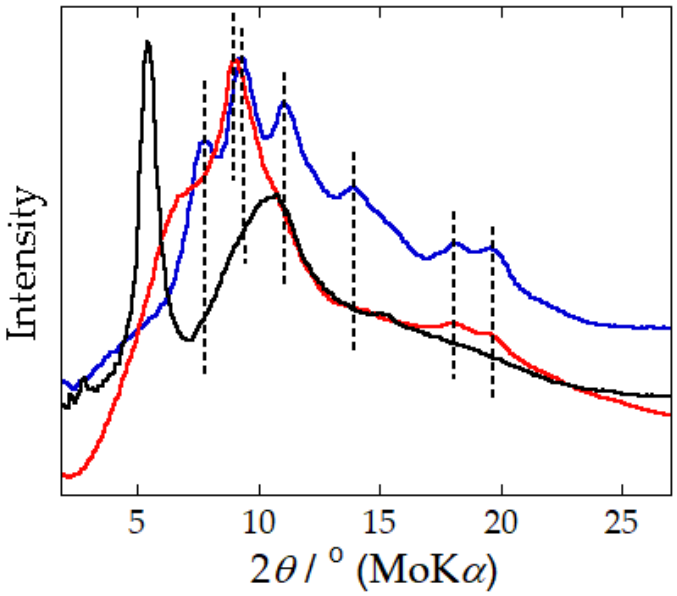


**Figure 3-8**

**WAXD $2\theta$-profiles of the dry SGF-gel (curve in blue), and $LF_{aq}$ (curve in black) and $SGF_{HFIP}$ (curve in red) as-cast films. The black, dotted lines indicate peaks assigned to the $\beta$-sheet structure.**

Thermal gravimetry (TG) and differential scanning calorimetry (DSC) profiles of the $LF_{aq}$ and $SGF_{HFIP}$ as-cast films were as shown in Figure 3-9. In the TG profiles, a significant loss in weight was detected at ~180 °C in the profile of the $SGF_{HFIP}$ as-cast film (indicated by a red dotted line in Figure 3-9a), but absent in that of the $LF_{aq}$ as-cast film.

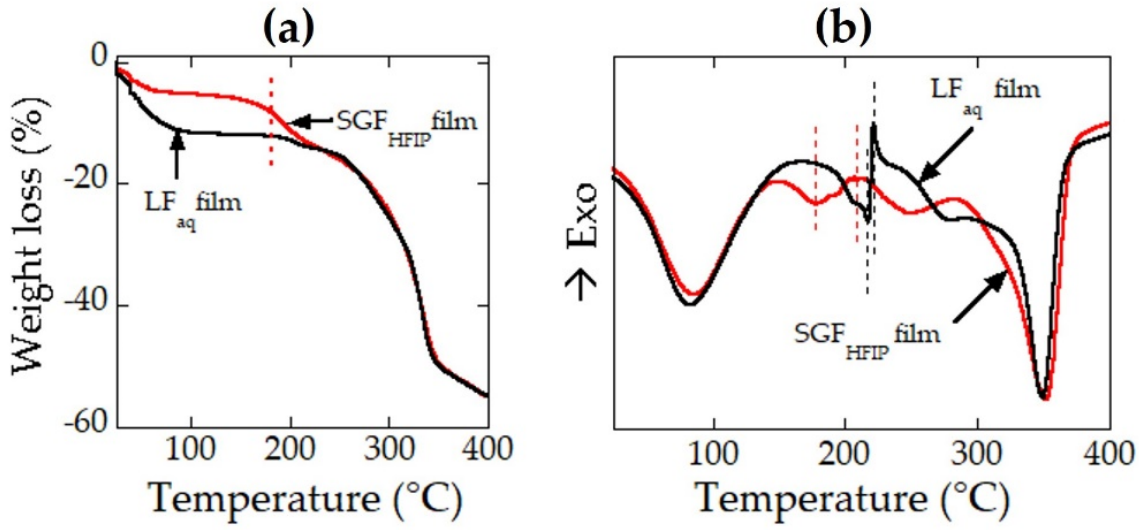


**Figure 3-9**

**Thermal gravimetry (TG) (a) and differential scanning calorimetry (DSC) (b) profiles of *S. c. ricini* $LF_{aq}$ (profile in black) and $SGF_{HFIP}$ (profile in red) as-cast films.**

In an earlier study on *B. mori* SGF, residual HFIP molecules were confirmed to form an $\alpha$-helix-HFIP complex [22,32] that was stable up to ~140 °C, which is higher than the boiling point of HFIP (~58.2 °C) [22]. This weight loss was considered to be due to the loss of residual HFIP, which was detected by FTIR (see Figure 3-10) in *S. c. ricini* $SGF_{HFIP}$ as-cast film, due to a similar phenomenon. On the other hand, the exothermic peak in the DSC profile of the $SGF_{HFIP}$ as-cast film was broader, and was detected at a slightly lower peak temperature (~200 °C) compared to that of the $LF_{aq}$ as-cast film (~220 °C) (Figure 3-9b). WAXD analyses shown in Figure 3-11 (and discussed thereafter) suggested the shift and broadening of this peak

to be due to closer packing and wider distribution, respectively, of the hexagonal packing of the $\alpha$-helical domains.

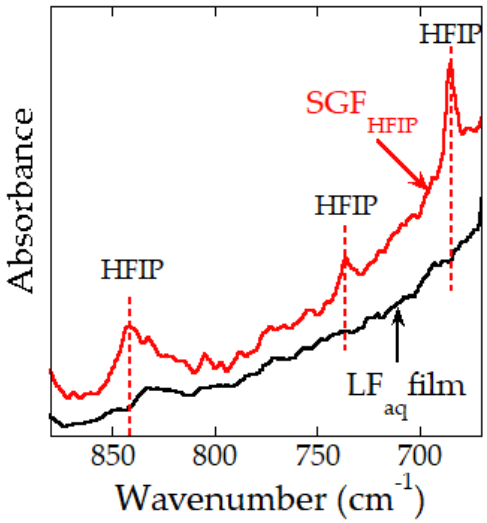


**Figure 3-10**

**FTIR spectra of *S. c. ricini* $LF_{aq}$ and $SGF_{HFIP}$ as-cast films showing the peaks assigned to HFIP.**

WAXD 2$\theta$-profiles of native fibre (same profile shown in Figure 3-1), as-cast and heat-treated $LF_{aq}$ and $SGF_{HFIP}$ films are shown in Figure 3-11. In chapter II, the $\alpha$-helical domains in the $LF_{aq}$ as-cast film were confirmed to self-assemble into an ordered aggregated state. This is well consistent with an earlier study by atomic force microscopy (AFM) in which *S. c. ricini* fibroin molecules were shown to self-assemble via electrostatic interactions to form highly ordered structures stabilized by intramolecular hydrogen bonds [36]. The profile of the $SGF_{HFIP}$ as-cast film (Figure 3-11b) had features essentially similar to those of the as-cast $LF_{aq}$ film (Figure 3-11a). However, the position of the (10-10) peak in the profile of the $LF_{aq}$ as-cast film (detected at $2\theta = 11.6°$; corresponding to $d = 7.6$ Å) (Figure 3-11a) became broad and shifted to a slightly wide-angle ($2\theta = 12.8°$; corresponding to $d = 7.0$ Å) in the profile of the $SGF_{HFIP}$ as-cast film (Figure 3-11b). The shift in peak position and peak broadening are considered to

be due to the closer packing but wider distribution of the ordered aggregation state of the $\alpha$-helices, as already mentioned in the DSC results. Both profiles showed a clear structural transition to the $\beta$-sheet structure due to heat treatment at 220 °C for 1 min (Figure 3-11a,b).

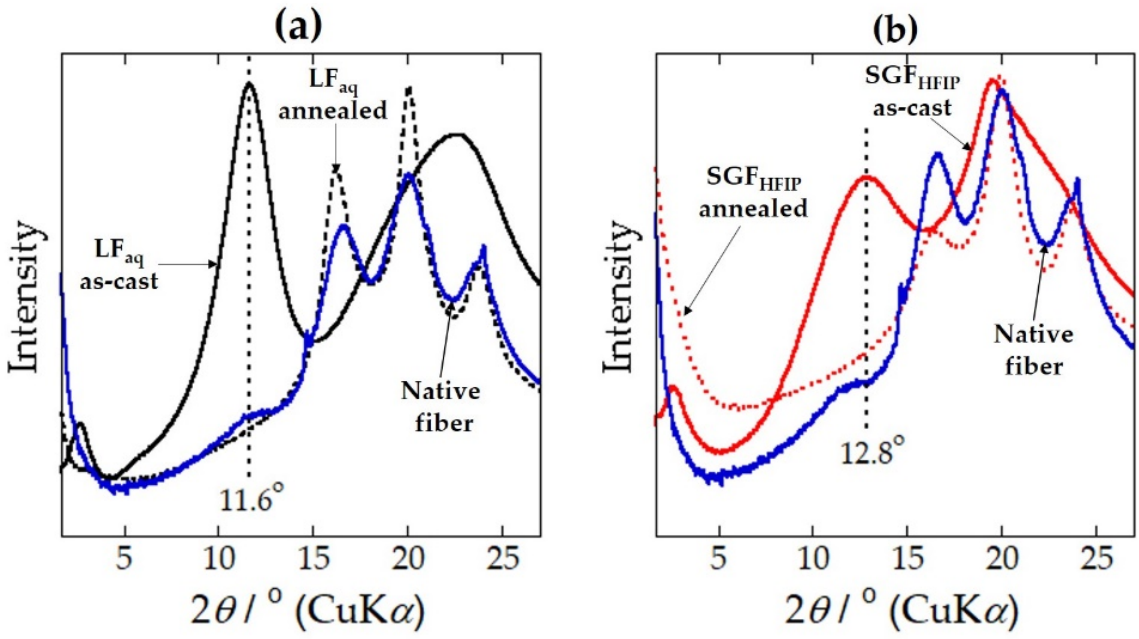


**Figure 3-11**

**WAXD 2$\theta$-profiles of *S. c. ricini* $LF_{aq}$ (a, black) and $SGF_{HFIP}$ (b, red) films, and native fibre (blue). The solid- and dotted-line profiles correspond to the as-cast and heat-treated (220 °C, 1 min) films, respectively.**

### 3.3.3. Structural Origin of the Water-Resistance Property of the $SGF_{HFIP}$ As-Cast Film

To clarify the structural origin of the water resistance property of the $SGF_{HFIP}$ as-cast film, rectangular portions of the water-soluble $LF_{aq}$ as-cast film were placed in a container saturated with HFIP gas at 23 ± 2 °C for 20 min. The shape of the HFIP-gas-treated film was not distorted, but the peaks assigned to HFIP were detected in the FTIR spectrum of the film. This indicated possible interaction between HFIP and the $\alpha$-helices in the $LF_{aq}$ as-cast film. However, the film remained water-soluble. This observation further suggested that the aggregated state of the $\alpha$-helices in the film treated with HFIP gas was not affected. Hence,

immediately the film was immersed in water, HFIP dissolved, its structure became similar to that of the $LF_{aq}$ as-cast film, and it dissolved.

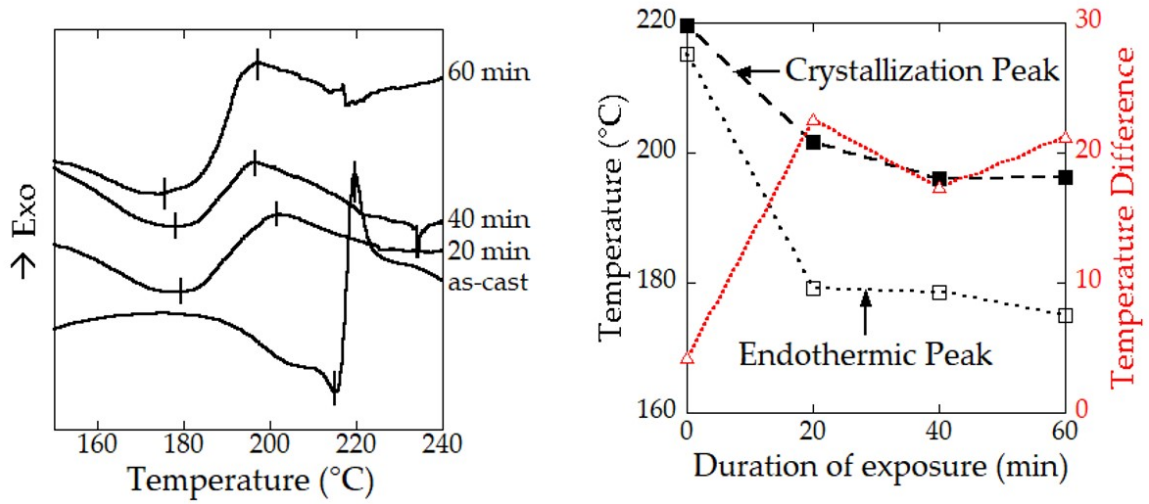


**Figure 3-12**

**DSC *β*-sheet crystallization peaks of the *S. c. ricini* $LF_{aq}$ film treated with HFIP gas at 23 °C for 20, 40, and 60 min. The panel on the right is a plot of the *β*-sheet crystallization peak temperatures against the duration of exposure to HFIP gas.**

The sharp *β*-sheet crystallization peak detected in the $LF_{aq}$ as-cast film broadened and was detected at a lower temperature in the DSC profile of the HFIP-gas-treated film as shown in Figure 3-12. Since surface adsorbed HFIP would easily evaporate during the DSC scan, this result confirms the interaction between HFIP and the ordered aggregated *α*-helices. To account for the peak shift and broadening detected in the profile of the film treated with HFIP gas, the gradual increase in temperature during the DSC scan was considered to increase the interaction between fibroin and HFIP molecules, eventually resulting in a structure similar to that of the $SGF_{HFIP}$ as-cast film. This implies that HFIP complexed with the *α*-helices, but the molecular movements in the solid-state are relatively low, hence the overall aggregated state is retained. This reasonably accounts for the broadening and shift of the endothermic peak even when the $LF_{aq}$ as-cast film was treated with HFIP gas under mild conditions. Further, similar results were

obtained when the $LF_{aq}$ as-cast film was exposed to HFIP gas for longer durations, and at higher temperatures (see Figures 3-12,13). However, higher temperatures (>50 °C) and longer exposure durations resulted in deformation and eventual dissolution of the film.

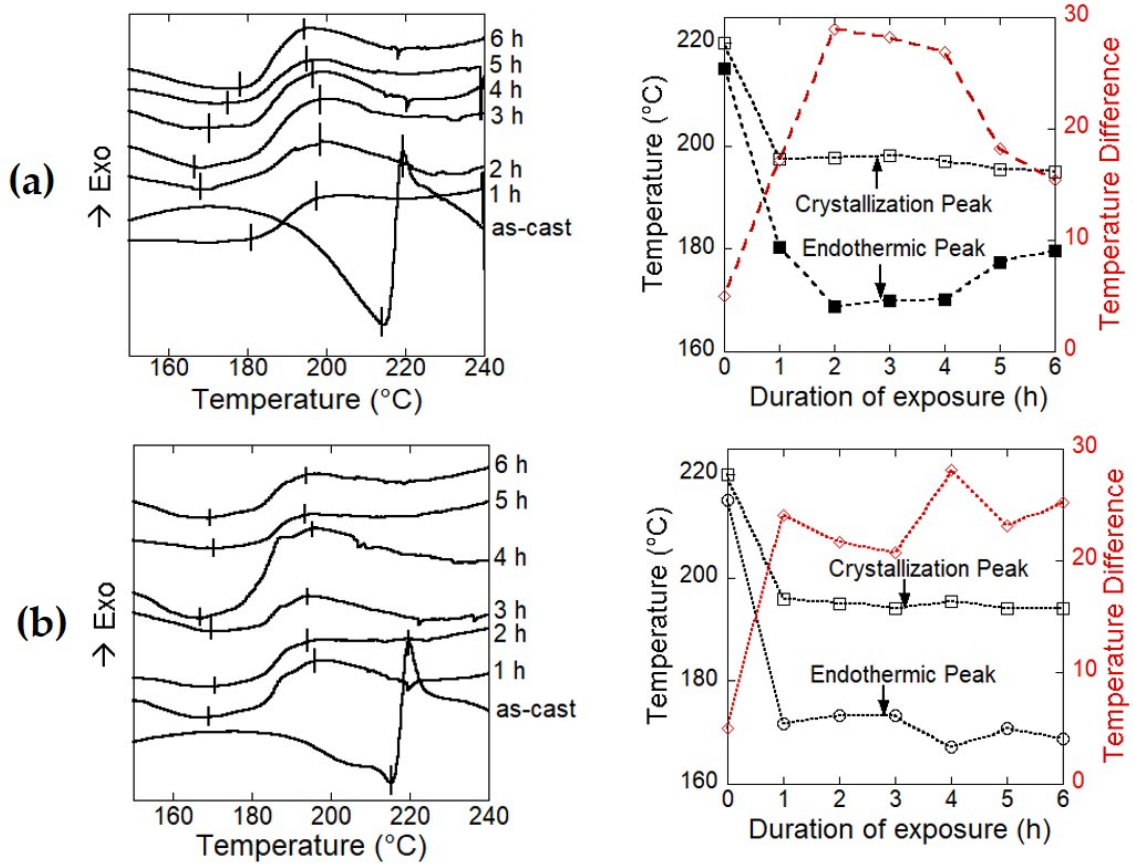


**Figure 3-13**

**DSC *β*-sheet crystallization profiles of the HFIP-gas-treated $LF_{aq}$ film at 30 (a) and 40 (b) °C for 1, 2, 3, 4, 5, and 6 h. The panels on the right are plots of the *β*-sheet crystallization peak temperatures against the duration of exposure to HFIP gas.**

The current results reveal a structure water-solubility relationship in the cast films whose mechanism is summarized in Figure 3-14. In the $LF_{aq}$ as-cast film, the interactions between the ordered aggregated *α*-helices (Figure 3-14a) are weak, and easily dissolve in water (Figure 3-14b).

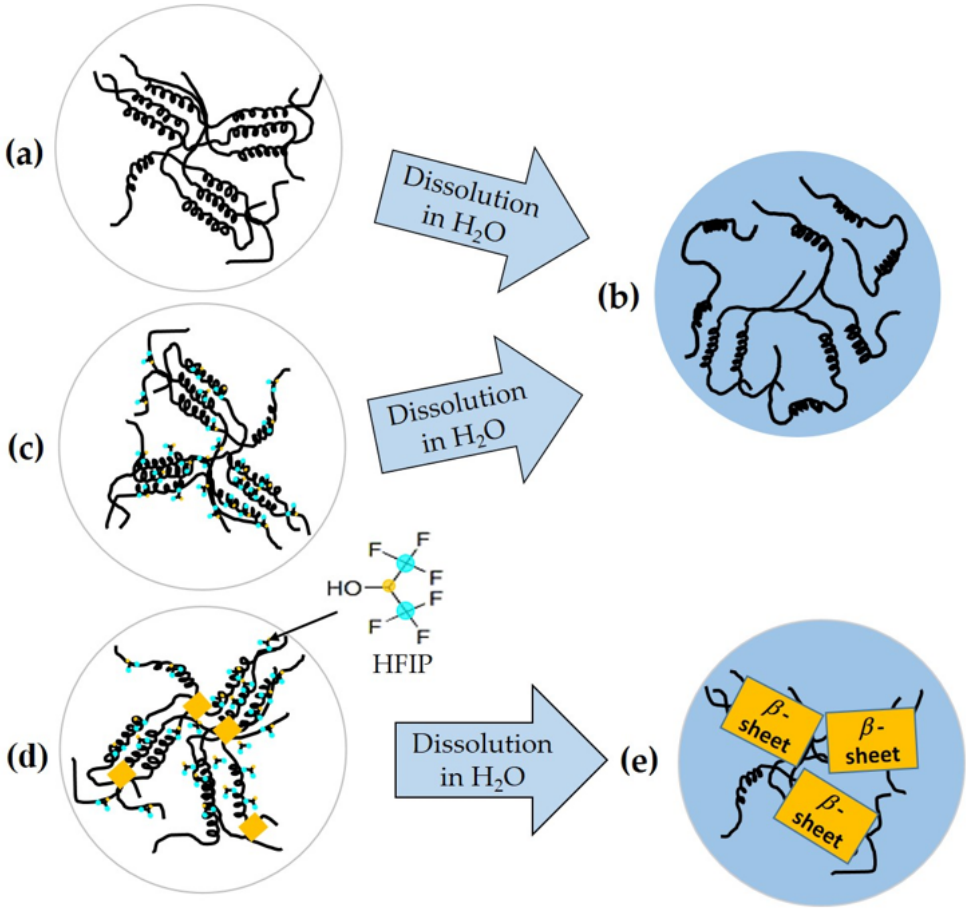


**Figure 3-14**

**The $LF_{aq}$ as-cast film has an ordered aggregated *α*-helix structure (a) that easily dissolves in water (b). When treated with HFIP gas, the aggregated *α*-helices in the $LF_{aq}$ as-cast film and HFIP molecules bind. However, due to low molecular movement in the solid state, the overall aggregation state of the *α*-helices is retained (c). The bound HFIP is easily removed by water, resulting in dissolution of the film. On the other hand, the 40%-EtOH-treatment induces imperfect *β*-sheet formation in the SGF-gel. As a result, the SGF-gel PSG is soluble in HFIP. However, some *β*-sheet structural memory remains, and the $SGF_{HFIP}$ as-cast film cast from a solution of the SGF-gel in HFIP has some *β*-sheet content which renders it water-resistant (d). Further, removal of residual HFIP in the $SGF_{HFIP}$ as-cast film by water renders it *β*-sheet-rich (e), indicating an occurrence of water induced *β*-sheet formation.**

When this film is treated with HFIP gas, the HFIP molecules and the $\alpha$-helices bind, but the molecular movements in the solid-state are relatively low and the "overall" aggregation state of the $\alpha$-helical domains is retained (Figure 3-14c). On being placed on a water surface, HFIP molecules easily dissolve due to their high affinity for water. As a result, the film treated with HFIP, now similar to the $LF_{aq}$ as-cast film, dissolves in water. On the other hand, the $SGF_{HFIP}$ as-cast film has some $\beta$-sheet content (indicated by yellow boxes in Figure 3-14d) that results from some $\beta$-sheet structural memory induced by treatment of SGF with 40%-EtOH. This renders the $SGF_{HFIP}$ as-cast film water-stable.

For use as a biomaterial, residual HFIP in the $SGF_{HFIP}$ as-cast film must be removed. Kameda et al. reported successful removal of residual HFIP from a film cast from hornet silk by rinsing in water [37].

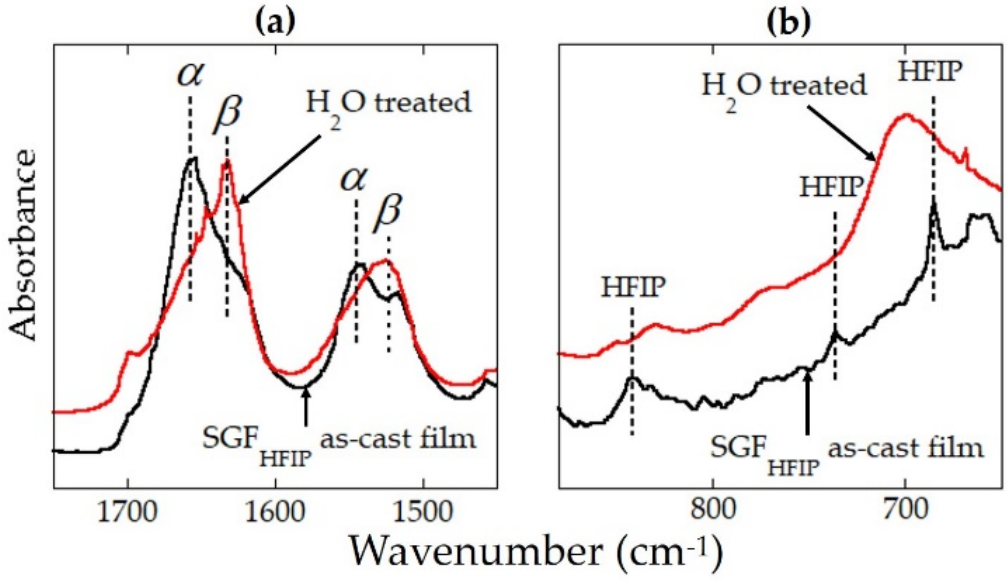


**Figure 3-15**

**FTIR spectra of *S. c. ricini* as-cast (spectrum in black) and water-treated (spectrum in red) $SGF_{HFIP}$ films. The vibrational bands in the amide I and II regions are shown in panel (a), whereas those assigned to HFIP are shown in panel (b).**

To evaluate if this strategy could be applicable in the current study, the $SGF_{HFIP}$ as-cast film was immersed in water for 12 h and its structural properties in the dry state were characterized by FTIR. FTIR spectra of the as-cast and water-treated $SGF_{HFIP}$ films were as shown in Figure 3-15. Owing to its high affinity for water, residual HFIP dissolved when the $SGF_{HFIP}$ as-cast film was immersed in water, as confirmed by the disappearance of the peaks assigned to HFIP (Figure 3-15b). The now-HFIP-free $SGF_{HFIP}$ film, thought to be similar to the $LF_{aq}$ as-cast film, did not dissolve in water, instead, a shift to higher wavenumbers of the amide I and II vibrational bands was detected in its FTIR spectrum in the dry state. This indicates an occurrence of water induced $\beta$-sheet formation from the aggregated $\alpha$-helix structure (Figure 3-15a).

$\beta$-sheet formation is well known to induce water-resistance in silk fibroin materials [38], hence the difference in water resistance between the $LF_{aq}$ and $SGF_{HFIP}$ as-cast films. Moreover, structural change, back to the $\alpha$-helical conformation, attributed to preferences of the polyalanine domains in hydrophobic and hydrophilic environments, respectively, upon drying of water-treated artificial spidroins has been reported [39,40]. However, the dominant structure of the water treated $SGF_{HFIP}$ film in the wet state remains unclarified and will be of interest in our future investigations.

### 3.3.4. Superior Wet-Drawability of the $SGF_{HFIP}$ As-Cast Film

Solvents and the initial conformation have been reported to influence some properties, especially the mechanical properties, of silk fibroin films [41]. It is also well documented that drawing results in $\alpha$-helix to $\beta$-sheet conformation transition in various types of silks [6,42–45]. With this understanding, and the $\beta$-sheet formation that occurs when the $SGF_{HFIP}$ as-cast film is immersed in water (discussed in the preceding section), possible slipping of the $\alpha$-helical chains during drawing is expected to be suppressed. This implies that the applied tension would be transmitted uniformly throughout the film. Therefore, we hypothesized that the $SGF_{HFIP}$ as-

cast film could be wet-drawn (while immersed in water). Moreover, since drawing is accompanied by a transition from the compact helical conformation to the elongated chain ($\beta$-sheet) structure, the films' maximum draw-ratio (DR) could be higher. Theoretically, the distance separating each complete turn along the helix axis is 5.4 Å (1.5 Å per residue), whereas a fully extended $\beta$-sheet structure corresponds to 3.4 Å per residue. Thus, a theoretical DR in changing from $\alpha$-helix to $\beta$-sheet would be ~2.27. To confirm these hypotheses, $SGF_{HFIP}$ and $LF_{aq}$ as-cast films treated with 80%-EtOH, to induce $\beta$-sheet formation, were drawn alongside the as-cast $SGF_{HFIP}$ film. Drawability, expressed as strain at break (%), attained for the films was as presented in Table 2.

**Table 2.** Strain at break (mean ± SD; %) of the as-cast $SGF_{HFIP}$ and 80%-EtOH-treated $SGF_{HFIP}$ and $LF_{aq}$ films (n = 19).

| Sample | Strain at Break (%) | | |
|---|---|---|---|
| | Minimum | Maximum | Average |
| $SGF_{HFIP}$ as-cast film | 180 | 230 | 202 ± 14 |
| 80%-EtOH-treated $SGF_{HFIP}$ cast film | 40 | 160 | 100 ± 33 |
| 80%-EtOH-treated $LF_{aq}$ cast film | 60 | 150 | 79 ± 29 |

The relative frequency distribution (%) of the maximum strain (strain at break) of the three kinds of silk fibroin films were as shown in Figure 3-16. Approximately 90% of the time, the $SGF_{HFIP}$ as-cast film could be successfully drawn to a DR >3 (corresponding to a maximum stain of >200%), whereas the 80%-EtOH-treated $LF_{aq}$ and $SGF_{HFIP}$ films could be drawn to maximum DR less than 2 (corresponding to a maximum strain of 100%). This was because the $SGF_{HFIP}$ as-cast film was initially $\alpha$-helix-rich, whereas the EtOH-treated $LF_{aq}$ and $SGF_{HFIP}$ films were $\beta$-sheet-rich, further supporting our interpretation. We interpret the $\alpha$-helix to $\beta$-sheet conformation transition during wet-drawing of the $SGF_{HFIP}$ cast film to be due to (1) stretching and (2) $\alpha$-helix to $\beta$-sheet conformation transition. $\beta$-sheet crystallization decreases

drawability of the $SGF_{HFIP}$ as-cast film, and the maximum DR achieved includes such a suppression effect, although other factors that may influence wet-drawability of the film such as film thickness, temperature, and drawing rate, are yet to be clarified. In earlier studies, drawing of semi-dried *S. c. ricini* silk dope gave a considerably high DR (~10) [6,44]. This is because the drawing force may break the interchain bonds resulting in extension and even slipping of the helical chains. Taking our results and the theoretical interpretation into account, slipping of molecular chains during drawing may largely account for the considerably high DR in earlier studies.

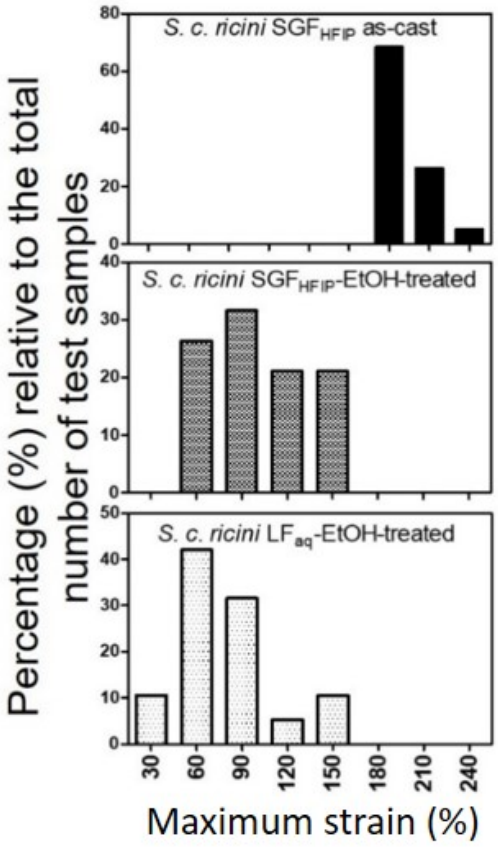


**Figure 3-16**

**Relative frequency distribution of the maximum strain (%) of the as-cast $SGF_{HFIP}$, and 80%-EtOH $SGF_{HFIP}$ and $LF_{aq}$ films.**

### 3.3.5. Industrial Prospects of the Current Fabrication Strategy

*S. c. ricini* silk glands are thin and flexuous, and peeling of the gland epithelium was time consuming. Due to these, further assessment was done on the possibility of obtaining a HFIP solution of SGF from the 40%-EtOH-treated PSG without peeling (see Table 1, $SGF_{HFIP}$, b). Portions of the 40%-EtOH-treated PSG were directly immersed in HFIP and the dissolved SGF was separated from the undissolved gland epithelium by filtration. As shown in Table 1, Ser residues in a film cast from the SGF-HFIP solution obtained ($SGF_{HFIP}$, b) were comparable, or even less than those in the conventional $LF_{aq}$ as-cast film, indicating better separation of the SGF-gel and gland epithelial layer. We expect that the application of this strategy will be useful in obtaining HFIP solutions of *S. c. ricini* SGF in an industrial scale.

## 2.4. Conclusions

In this chapter, a transparent, flexible, $\alpha$-helix-rich, and water-insoluble as-cast film was successfully fabricated from *S. c. ricini* silk fibroin without post-treatment. This was attained using aqueous 40%-EtOH solidification (gelation) of fibroin in the lumen of the posterior section of silk glands freshly extracted from late fifth instar *S. c. ricini* larvae. This treatment enabled the separation of pure fibroin from the rest of the silk gland. The fibroin obtained was soluble in HFIP at room temperature, implying that the treatment only induced an "imperfect $\beta$-sheet structure". Unlike the conventional film cast from aqueous liquid fibroin, the one cast from the SGF-HFIP solution obtained ($SGF_{HFIP}$ as-cast film) was insoluble in water. This was attributed to $\beta$-sheet structural memory, that is, the $SGF_{HFIP}$ as-cast film contains some $\beta$-sheet structure, hence the water-insoluble property.

When the $SGF_{HFIP}$ as-cast film is rinsed in water, residual HFIP dissolves and the film becomes $\beta$-sheet-rich. This indicates the occurrence of "water-induced $\beta$-sheet formation". Despite the transformation of the $\alpha$-helix-rich $SGF_{HFIP}$ cast film into being $\beta$-sheet rich when rinsed in water, the Ala-Aa residues in the $\alpha$-helical domains in the initial hexagonally packed

structure aligned face to face and easily transform into a highly regular *β*-sheet structure compared to that attained in *B. mori* silk fibroin. Moreover, the film has superior drawability and is potentially applicable in more versatile applications. This is a new insight that may be utilized in fabrication of films with better physical properties.

These results reveal an important structure water-solubility relationship in the α-helix-rich films cast from *S. c. ricini* silk fibroin, that is, the existence of a small amount of *β*-sheet structure in the *α*-helix rich domains of the $SGF_{HFIP}$ as-cast film significantly influences its solubility in water. Based on these findings, a plausible model of the mechanism leading to insolubility in water of the $SGF_{HFIP}$ as-cast film is proposed. This water-resistant film is relatively easy to fabricate and may be attractive as a biomaterial. Further, we expect this fabrication strategy to be applicable to the other kinds of wild silkworm silk.

**References**


[1] Sezutsu, H. & Yukuhiro, K. The complete nucleotide sequence of the Eri-silkworm (*Samia cynthia ricini*) fibroin gene. *J. Insect Biotechnol. Sericol.* **83**, 59–70 (2014).

[2] Asakura, T. & Nakazawa, Y. Structure and structural changes of the silk fibroin from *Samia cynthia ricini* using nuclear magnetic resonance spectroscopy. *Macromol. Biosci.* **4**, 175–185 (2004).

[3] Zhou, C. Z., Confalonieri, F., Jacquet, M., Perasso, R., Li, Z. G. & Janin, J. Silk fibroin: Structural implications of a remarkable amino acid sequence. *Proteins* **44**, 119–122 (2001).

[4] Suzuki, Y., Yamazaki, T., Aoki, A., Shindo, H. & Asakura, T. NMR study of the structures of repeated sequences, GAGXGA (X = S, Y, V), in *Bombyx mori* liquid silk. *Biomacromolecules* **15**, 104–112 (2014).

[5] van Beek, J. D., Beaulieu, L., Schäfer, H., Demura, M., Asakura, T. & Meier, B. H. Solid-state NMR determination of the secondary structure of *Samia cynthia ricini* silk. *Nature* **405**, 1077–1079 (2000).

[6] Yang, M., Yao, J., Sonoyama, M. & Asakura, T. Spectroscopic characterization of heterogeneous structure of *Samia cynthia ricini* silk fibroin induced by stretching and molecular dynamics simulation. *Macromolecules* **37**, 3497–3504 (2004).

[7] Rajkhowa, R., Wang, L., Kanwar, J. R. & Wang, X. Molecular weight and secondary structure change in Eri silk during alkali degumming and powdering. *J. Appl. Polym. Sci.* **119**, 1339–1347 (2011).

[8] Chattopadhyay, D., Chakraborty, A. & Chatterjee, S. M. Studies on degumming of eri silk cocoons. *J. Text. Inst.* **108**, 1327–1339 (2017).

[9] Silva, S. S., Oliveira, N. M., Oliveira, M. B., da Costa, D. P. S., Naskar, D., Mano, J. F., Kundu, S. C. & Reis, R. L. Fabrication and characterization of Eri silk fibres-based sponges for biomedical application. *Acta Biomater.* **32**, 178–189 (2016).

[10] Dutta, S., Talukdar, B., Bharali, R., Rajkhowa, R. & Devi, D. Fabrication and characterization of biomaterial film from gland silk of Muga and Eri silkworms. *Biopolymers* **99**, 326–333 (2013).

[11] Perotto, G., Zhang, Y., Naskar, D., Patel, N., Kaplan, D. L. & Kundu, S. C. Omenetto, F.G. The optical properties of regenerated silk fibroin films obtained from different sources. *Appl. Phys. Lett.* **111**, 103702 (2017).

[12] Yoshioka, T., Hata, T., Kojima, K., Nakazawa, Y. & Kameda, T. Fabrication scheme for obtaining transparent, flexible, and water-insoluble silk films from apparently dissolved silk-gland fibroin of *Bombyx mori* silkworm. *ACS Biomater. Sci. Eng.* **3**, 3207–3214 (2017).

[13] Lu, Q., Hu, X., Wang, X., Kluge, J. A., Lu, S., Cebe, P. & Kaplan, D. L. Water-insoluble silk films with silk I structure. *Acta Biomater.* **6**, 1380−1387 (2010).

[14] Jin, H. J., Park, J., Karageorgiou, V., Kim, U. J., Valluzzi, R., Cebe, P. & Kaplan, D. L. Water-stable silk films with reduced *β*-sheet content. *Adv. Funct. Mater*. **15**, 1241−1247 (2005).

[15] Hu, X., Shmelev, K., Sun, L., Gil, E. S., Park, S. H., Cebe, P. & Kaplan, D. L. Regulation of silk material structure by temperature- controlled water vapor annealing. *Biomacromolecules* **12**, 1686− 1696 (2011).

[16] Yao, D., Liu, H. & Fan, Y. Fabrication of water-stable silk fibroin scaffolds through self-assembly of proteins. *RSC Adv.* **6**, 61402− 61409 (2016).

[17] Minoura, N., Aiba, S., Higuchi, M., Gotoh, Y., Tsukada, M. & Imai, Y. Attachment and growth of fibroblast cells on silk fibroin. *Biochem. Biophys. Res. Commun.* **208**, 511–516 (1995).

[18] Borkner, C. B., Elsner, M. B., & Scheibel, T. Coatings and films made of silk proteins. *ACS Appl. Mater. Interfaces* **6**, 15611–15625 (2014).

[19] Fedic, R., Zurovec, M. & Sehnal, F. The silk of Lepidoptera, *J. Insect Biotechnol. Sericol.* **71**, 1–15 (2002).

[20] Freddi, G., Monti, P., Nagura, M., Gotoh, Y. & Tsukada, M. Structure and molecular conformation of Tussah silk fibroin films: Effect of heat treatment. *J Polym. Sci. Polym. Phys.* **35**, 841–847 (1997).

[21] Guo, C., Zhang, J., Jordan, J. S., Wang, X., Henning, R. W. & Yarger, J. L. Structural comparison of various silkworm silks: An insight into the structure–property relationship. *Biomacromolecules* **19**, 906–917 (2018).

[22] Yoshioka, T., Tashiro, K. & Ohta, N. Molecular orientation enhancement of silk by the hot-stretching-induced transition from $\alpha$-helix-HFIP complex to $\beta$-sheet. *Biomacromolecules* **17**, 1437–1448 (2016).

[23] Yoshioka, T. & Kameda, T. X-ray scattering analyses quantitatively revealed periodic hierarchical structure of polyalanine $\beta$-sheet and non-polyalanine amorphous domains in *Antheraea assamensis* (Muga) silk. *J. Silk Sci. Tech. Jpn.* **27**, 95–101 (2019).

[24] Roccatano, D., Fioroni, M., Zacharias, M., & Colombo, G. Effect of hexafluoroisopropanol alcohol on the structure of melittin: A molecular dynamics simulation study. *Protein Sci.* **14**, 2582–2589 (2005).

[25] Gast, K., Siemer, A., Zirwer, D., & Damaschun, G. Fluoroalcohol-induced structural changes of proteins: some aspects of cosolvent-protein interactions. *Euro. Biophys. J.* **30**, 273–283 (2001).

[26] Hong, D. P., Hoshino, M., Kuboi, R., & Goto, Y. Clustering of fluorine-substituted alcohols as a factor responsible for their marked effects on proteins and peptides. *J. Am. Chem. Soc.* **121**, 8427–8433 (1999).

[27] Lock, R. L. Process for making silk fibroin fibres. US Patent 5,252,285. 12 October 1993.

[28] Ha, S. W., Asakura, T. & Kishore, R. Distinctive influence of two hexafluoro solvents on the structural stabilization of *Bombyx mori* silk fibroin protein and its derived peptides: $^{13}$C NMR and CD studies. *Biomacromolecules* **7**, 18–23 (2006).

[29] Zhao, C., Yao, J., Masuda, H., Kishore, R. & Asakura, T. Structural characterization and artificial fibre formation of *Bombyx mori* silk fibroin in hexafluoro-iso-propanol solvent system. *Biopolymers* **69**, 253–259 (2003).

[30] Zarkoob, S., Eby, R. K., Reneker, D. H., Hudson, S. D., Ertley, D. & Adams, W. W. Structure and morphology of electrospun silk nanofibres. *Polymer* **45**, 3973−3977 (2004).

[31] Wang, Q., Chen, Q., Yang, Y. & Shao, Z. Effect of various dissolution systems on the molecular weight of regenerated silk fibroin. *Biomacromolecules* **14**, 285–289 (2013).

[32] Drummy, L. F., Phillips, D. M., Stone, M. O., Farmer, B. L. & Naik, R. R. Thermally induced $\alpha$-helix to $\beta$-sheet transition in regenerated silk fibres and films. *Biomacromolecules* **6**, 3328–3333 (2005).

[33] Spek, E. J., Olson, C. A., Shi, Z. & Kallenbach, N. R. Alanine is an intrinsic $\alpha$-helix stabilizing amino acid. *J. Am. Chem. Soc.* **121**, 5571–5572 (1999).

[34] Nakazawa, Y. & Asakura, T. Structure determination of a peptide model of the repeated helical domain in *Samia cynthia ricini* silk fibroin before spinning by a combination of advanced solid-state NMR methods. *J. Am. Chem. Soc.* **125**, 7230–7237 (2003).

[35] Kluge, J. A., Kahn, B. T., Brown, J. E., Omenetto, F. G. & Kaplan, D. L. Optimizing molecular weight of lyophilized silk as a shelf-stable source material. *ACS Biomater. Sci. Eng.* **4**, 595–605 (2016).

[36] Inoue, S. I., Tsuda, H., Tanaka, T., Kobayashi, M., Magoshi, Y. & Magoshi, J. Nanostructure of natural fibrous protein: In vitro nanofabric formation of *Samia cynthia ricini* wild silk fibroin by self-assembling. *Nano Lett.* **3**, 1329–1332 (2003).

[37] Kameda, T., Kojima, K., Miyazawa, M. & Fujiwara, S. Film formation and structural characterization of silk of the hornet *Vespa simillima xanthoptera* Cameron. *Z Naturforsch.* **60**, 906–914 (2005).

[38] Magoshi, J., Magoshi, Y. & Nakamura, S. Mechanism of fibre formation of silkworm. In *Silk Polymers*; ACS Symposium Series; American Chemical Society: Washington, DC, USA, Chapter 25, Volume 544, 292–310 (1993).

[39] Otikovs, M., Andersson, M., Jia, Q., Nordling, K., Meng, Q., Andreas, L. B.; Pintacuda, J., Johansson, J., Rising, A. & Jaudzems, K. Degree of biomimicry of artificial spider silk spinning assessed by NMR spectroscopy. *Angew. Chemie* **56**, 12571–12575 (2017).

[40] Levy, Y., Jortner, J., Becker, O. M. Solvent effects on the energy landscapes and folding kinetics of polyalanine. *PNAS* **98**, 2188–2193 (2001).

[41] Spiess, K., Ene, R., Keenan, C. D., Senker, J., Kremer, F. & Scheibel, T. Impact of initial solvent on thermal stability and mechanical properties of recombinant spider silk films. *J. Mater. Chem.* **21**, 13594–13604 (2011).

[42] Yoshioka, T., Kameda, T., Tashiro, K. & Schaper, A. K. Transformation of coiled *α*-helices into *cross-β*-sheets superstructure. *Biomacromolecules* **18**, 3892–3903 (2017).

[43] Kameda, T., Kojima, K., Togawa, E., Sezutsu, H., Zhang, Q., Teramoto, H. & Tamada, Y. Drawing-induced changes in morphology and mechanical properties of hornet silk gel films. *Biomacromolecules* **11**, 1009–1018 (2010).

[44] Rousseau, M. E., Beaulieu, L., Lefèvre, T., Paradis, J., Asakura, T. & Pèzolet, M. Characterization by Raman microspectroscopy of the strain-induced conformational transition in fibroin fibres from the silkworm *Samia cynthia ricini*. *Biomacromolecules* **7**, 2512–2521 (2006).

[45] Tucker, C. L., Jones, J. A., Bringhurst, H. N., Copeland, C. G., Addison, J. B., Weber, W. S., Mou, Q., Yarger, J. L. & Lewis, R. V. Mechanical and physical properties of recombinant spider silk films using organic and aqueous solvents. *Biomacromolecules* **15**, 3158–3170 (2014).

## Chapter IV

## Overall conclusions

Silk fibroins have in the recent past attracted increasing interest for use as biomaterials owing to their attractive properties such as excellent mechanical properties, biocompatibility, biodegradability, as well as abundant yields in nature. However, to-date, wild silkworm fibroins remain largely unexplored. In view of these, the current study focussed on the now domesticated wild silkworm, *S. c. ricini*, silk fibroin. Moreover, due to differences in the primary structure, conventional processing strategies used for *B. mori* silk fibroin are not applicable or optimum for *S. c. ricini* silk fibroin. Herein, the author reports on the conformational characterization and strategies for controlled processing of *S. c. ricini* silk fibroin, an important step towards efficient utilization of wild silks.

In chapter II, the aggregation state of the residual $\alpha$-helical domains in the poly-L-alanine regions, and their influence on the mechanical deformation behavior of *S. c. ricini* native fibre was clarified. The $\alpha$-helical domains were shown to be ordered, that is, they aggregate with a hexagonal packing in the aqueous solution state, some of which remain during the natural spinning process. Herein, the untransformed $\alpha$-helical domains are referred to as the residual $\alpha$-helices. X-ray scattering and DSC analyses revealed occurrence of a structural transition of the residual $\alpha$-helices to the $\beta$-sheet structure, accompanied by disappearance of the characteristic plateau region often observed in the force-strain curve, due to heat-treatment at ~220 °C. The broad peak at around 3.9 Å in the $2\theta$-profiles of the $LF_{aq}$ as-cast film and native fibre revealed that the residual $\alpha$-helical domains in the otherwise typically $\beta$-sheet-rich native fibre are aggregated in a hexagonal packing, though not perfectly crystallized. Further, based on X-ray scattering analyses before and after tensile stretching of *S. c. ricini* native silk, a direct connection between the plateau region and the $\alpha$-helix to $\beta$-sheet structural transition was

confirmed. These findings demonstrate the importance of the poly-L-alanine sequence regions in fibre structure formation and their influence on the tensile deformation behavior of *S. c. ricini* silk, features believed to be similar in other saturniid silks. We believe the residual ordered $\alpha$-helices to be strategically and systematically designed by *S. c. ricini* silkworms to impart flexibility in native silk fibre. It is anticipated that these knowledge forms a basis for fruitful strategies in the design and development of amino acid sequences for artificial silks with desired mechanical properties.

Towards effective utilization of the unique mechanical properties, biocompatibility and promising applications of *S. c. ricini* silk fibroin, a cast film that is both $\alpha$-helix-rich and water-stable was successfully fabricated from silk gland fibroin without post-treatment. This solves the challenge of the need of post-treatment in conventional films which often renders the cast films less flexible or even brittle. The strategy for fabrication of water-stable films from S. *c. ricini* silk gland fibroin entailed the use of aqueous ethanol induced gelation of fibroin in the posterior silk glands, to enable separation of fibroin from the rest of the silk gland. When dissolved in HFIP, the SGF-gel gave a solution from which a transparent, flexible, and water-insoluble film ($SGF_{HFIP}$) was cast. Detailed structural characterization of the $SGF_{HFIP}$ as-cast film was carried out and compared to a conventional, water-soluble film cast from $LF_{aq}$. FTIR and $^{13}C$ solid-state NMR analyses revealed both cast films to be $\alpha$-helix-rich. However, gelation of silk gland fibroin induced by the 40%-EtOH-treatment resulted in an imperfect $\beta$-sheet structure. As a result, the SGF-gel was soluble in HFIP, but some $\beta$-sheet structural memory remains, and the $SGF_{HFIP}$ as-cast film obtained has some $\beta$-sheet content which renders it water-resistant. In water, residual HFIP dissolves and the film becomes $\beta$-sheet-rich, indicating an occurrence of water-induced $\beta$-sheet formation. Based on these, a plausible model of the mechanism leading to the difference in water resistance of the $LF_{aq}$ and $SGF_{HFIP}$ as-cast

films is proposed and we expect this fabrication strategy to be applicable to the other kinds of wild silkworm silk.

These results reveal clear structure water property relationships in *S. c. ricini* native fiber and silk fibroin cast films that may offer useful insights towards tunable fabrication of novel biomaterials. Further research on the cast films fabricated in this study entailing properties such as cell adhesion activity and biodegradability will be required as another step towards their utilization as biomaterials. Moreover, it is anticipated that this knowledge will form a basis for fruitful strategies in the design and development of silk fibroin - based biomaterials as well as amino acid sequences for artificial silks with desired mechanical and biomedical properties.

**Acknowledgements**

First, I would like to thank God for his grace and providence that has seen me this far.

My sincere thanks go to my supervisor Professor Y. Nakazawa of the Department of Biotechnology and Life Science, Graduate School of Engineering, Tokyo University of Agriculture and Technology for his guidance throughout my studies.

I thank Dr. T. Kameda, Leader of the Silk Materials Research Unit and chief advisor of the SATREPS "Project for development of sericulture research by applying biological resources and molecular genetics" for allowing me to be part of the project and utilize rehouses in his Laboratory.

I greatly appreciate Dr. T. Yoshioka of the Institute of Agrobiological Sciences (NARO) for his guidance, careful reviews, helpful suggestions, thoughtful criticism and advice throughout my project. I owe a lot to him for taking his valuable time to guide and share with me his fast knowledge on silk which was key in the improvement and accomplishment of this piece of work.

I am grateful to the staff of the Silk Materials Research Unit, Division of Biotechnology, Institute of Agrobiological Sciences, National Agriculture and Food Research Organization (NARO) for their kind support in rearing the *S. c. ricini* silkworms.

I also thank Messrs. W. Kawai, Y. Hagiwara, K. Matsunaga, and T. Ogawa of Central Glass Co., Ltd (Tokyo, Japan), for their kind support with GPC analyses.

This study was supported by the Japan Science and Technology Agency (JST) and Japan International Cooperation Agency (JICA), Science and Technology Research Partnership for Sustainable Development (SATREPS) 2016-2021, grant number 18-161011166. I thank, Kenya Agricultural and Livestock Research Organization (KALRO), NARO, JICA, JST and the governments of Kenya and Japan for the financial support.

My appreciation also goes to my family and friends for their patience, understanding and financial and material support throughout the time of this study.

I dedicate this dissertation to the memory of my late grandmother, Z. N. Nyang'arisa.

February 12th, 2020

Kelvin Moseti OKONG'O

## Publications

[1] Moseti, K. O., Yoshioka, T., Kameda, T. & Nakazawa, Y. Aggregation state of residual $\alpha$-helices and their influence on physical properties of *S. c. ricini* native fibre. *Molecules* **24**, 3471 (2019).

[2] Moseti, K. O., Yoshioka, T., Kameda, T. & Nakazawa, Y. Structure water-solubility relationship in $\alpha$-helix-rich films cast from aqueous and 1,1,1,3,3,3-hexafluoro-2-propanol solutions of *S. c. ricini* silk fibroin. *Molecules* **24**, 3945 (2019).

## Other Publications

[1] Yoshioka, T., Kameda, T., Moseti, K. O., & Nakazawa, Y. Development of silk materials from *Samia cynthia ricini* (Eri-silk), *Book of abstracts, The 64$^{th}$ Japan Silk Association Research Conference and Ordinary General Meeting, Tsukuba, Japan, May 18-19, 2017.*

[2] Moseti, K. O., Yoshioka, T., Kameda, T., & Nakazawa, Y. Water-stable *Samia cynthia ricini* silk gland fibroin films for biomedical applications, *Book of abstracts, Tsukuba Biomedical Engineering Collaboration Forum, Tsukuba, Japan, January 26, 2018.*

[3] Moseti, K. O., Yoshioka, T., Kameda, T., & Nakazawa, Y. Fabrication of transparent, flexible and water-insoluble, non-mulberry silk fibroin films, *Book of abstracts, The 2018 Fibre Society's Spring Conference. Tokyo, Japan, June 12-14, 2018.*

[4] Moseti, K. O., Yoshioka, T., Kameda, T., & Nakazawa, Y. Solvent- and drawing-dependent transitions in silk gland fibroin materials, *Book of abstracts, Tsukuba Biomedical Engineering Collaboration Forum, Tsukuba, Japan, January 25, 2019.*

[5] Moseti, K. O., Yoshioka, T., Kameda, T., & Nakazawa, Y. A mild dissolution strategy for cocoon silk fibroin from the non-mulberry silkworm, *Samia cynthia ricini*, *Book of abstracts, The 2019 Fibre Society's Spring Conference. Tokyo, Japan, June 5-7, 2019.*

[6] Moseti, K. O., Yoshioka, T., Kameda, T., & Nakazawa, Y. Structural origin of the water-resistance of films cast from *S. c. ricini* silk fibroin solutions in 1,1,1,3,3,3-hexafluoro-2-propanol. *Book of abstracts, The 25th International Congress on Sericulture and Silk Industry, Tsukuba, Japan, November 19-22, 2019.*